Retrieving UV-VIS Spectral Single-scattering Albedo of Absorbing Aerosols above Clouds from Synergy of ORACLES Airborne and A-train Sensors

5   Hiren T Jethva[1,2], Omar Torres[2], Richard Anthony Ferrare[3], Sharon P Burton[3], Anthony L Cook[3], David B Harper[3], Chris A Hostetler[3], Jens Redemann[4], Vinay Kayetha[5], Samuel LeBlanc[6], Kristina Pistone[6], Logan Mitchell[4], Connor J Flynn[4]

[1]Morgan State University, Baltimore, MD, United States
10 [2]NASA Goddard Space Flight Center, Greenbelt, MD, United States
[3]NASA Langley Research Center, Hampton, VA, United States
[4]University of Oklahoma, Norman, OK, United States
[5]Science Systems and Applications, Inc., Lanham, MD, United States
[6]Bay Area Environmental Research Institute, Moffett Field, CA, United States

Correspondence to: Hiren Jethva (hiren.t.jethva@nasa.gov)

Abstract. Inadequate knowledge about the complex microphysical and optical processes of the aerosol-cloud system severely restricts our ability to quantify the resultant impact on climate. Contrary to the negative radiative forcing (cooling) exerted by aerosols in cloud-free skies over dark surfaces, the absorbing aerosols, when lofted over the
20 clouds, can potentially lead to significant warming of the atmosphere. The sign and magnitude of the aerosol radiative forcing over clouds are determined mainly by the amount of aerosol loading, the absorption capacity of aerosols or single-scattering albedo (SSA), and the brightness of the underlying cloud cover. In the satellite-based algorithms that use measurements from passive sensors, the assumption of aerosol SSA is known to be the largest source of uncertainty in quantifying above-cloud aerosol optical depth (ACAOD). In this paper, we introduce a novel synergy algorithm
25 that combines direct airborne measurements of ACAOD and the top-of-atmosphere (TOA) spectral reflectance from OMI and MODIS sensors of NASA's A-train satellites to retrieve 1) SSA of light-absorbing aerosols lofted over the clouds, and 2) aerosol-corrected cloud optical depth (COD). Radiative transfer calculations show a marked sensitivity of the TOA measurements to ACAOD, SSA, and COD, further suggesting that the availability of accurate ACAOD allows retrieval of SSA for above-cloud aerosols scenes using the 'color ratio' algorithm developed for satellite sensors
30 carrying ultraviolet (UV) and visible-near-IR (VNIR) wavelength bands. The proposed algorithm takes advantage of airborne measurements of ACAOD acquired from the High-spectral Resolution Lidar-2 (HSRL-2) and Spectrometer for Sky-Scanning, Sun-Tracking Atmospheric Research (4STAR) Sunphotometer operated during the ORACLES (ObseRvations of Aerosols above CLouds and their intEractionS) field campaign (September 2016, August 2017, and October 2018) over the southeastern Atlantic Ocean, and synergize them with TOA reflectance from OMI and MODIS
35 to derive spectral SSA in the near-UV (354-388 nm) and VIS-near-IR (470-860 nm), respectively. When compared against the ORACLES airborne remote sensing and in situ measurements and the inversion dataset of ground-based AERONET over land, the retrieved spectral SSAs from the satellites, on average, were found to be higher overall by ~0.01-0.02—a positive bias still within the uncertainties involved in all these inversion datasets. The sensitivity

analysis quantifying theoretical uncertainties in the retrieved SSA shows that errors in the measured ACAOD, aerosol layer height, and the ratio of the imaginary part of the refractive index (spectral dependence) of aerosols by 20%, 1 km, and 10%, respectively, produce an error in the retrieved SSA by 0.017 (0.01), 0.008 (0.001), and 0.03 (0.005) at 388 (470) nm. The development of the proposed aerosol-cloud algorithm implies a possible synergy of CALIOP lidar and OMI-MODIS passive sensors to deduce a global product of ACAOD and SSA. The availability of such global dataset can help constrain the climate models with the much-needed observational estimates of the radiative effects of aerosols in cloudy regions and expand our ability to study aerosol effects on clouds.

1   INTRODUCTION

Aerosol-cloud interactions continue to be the largest source of uncertainty in predicting the role of aerosols on climate (IPCC, 2021). One of the main hurdles is the lack of comprehensive knowledge about the complex microphysical and optical processes of the aerosol-cloud system that govern the resultant impact on the regional and global climate systems. The transoceanic transport of fine-mode aerosol from biomass burning and coarse-mode mineral aerosols from dust storms have been well documented using ground and remote sensing observations (Prospero et al., 2002; Kaufman et al., 2005; Chand et al., 2008; Torres et al., 2012). The long-range transport of aerosols often takes place above low-level clouds. Lofted layers of aerosols above the boundary layer and over the clouds have a longer lifetime in prevailing wind conditions across the oceans and therefore have a higher chance of long-range transport at intercontinental scales. Elevated aerosol layers over clouds are commonly observed during field campaigns (Zuidema et al., 2016; Redemann et al., 2021) as well as from satellites (Chand et al., 2008; Wilcox et al., 2009; Torres et al., 2012; Jethva et al., 2018) over several regions of the world. Unlike the cloud-free conditions in which aerosols generally produce a cooling effect on climate, the presence of elevated layers of absorbing aerosols over clouds can potentially exert a large positive forcing through enhanced atmospheric heating resulting from aerosol-cloud radiative interactions (Keil and Haywood, 2003; Chand et al., 2009; de Graaf et al., 2012; Zhang et al., 2016; Kacenelenbogen et al., 2019). Thus, if not considered in the global estimates, aerosols lofted over the cloud can potentially introduce a large uncertainty in the net aerosol forcing estimates. Even the sign of aerosol forcing will remain unknown until we can produce global, reliable quantitative observations of aerosol loading above clouds.

Eswaran et al. (2015), using CALIOP, MODIS, and OMI data for the Bay of Bengal region, showed that the critical cloud fraction (CCF)—the cloud fraction at which the sign of aerosol radiative forcing switches from negative (cooling) to positive (warming), is strongly dependent on the single-scattering albedo (SSA) of aerosols above the cloud. A seasonal shift in SSA from about 0.97 to 0.9 reduced the CCF from 0.28 to 0.13. In addition to their direct effects, absorbing aerosols above the clouds can produce a semi-direct effect on the cloud properties underlying the absorbing aerosol layer (Wilcox, 2012). On the aerosol modeling aspect, different climate models treat aerosol-cloud interaction processes differently, which results in the largest inter-model discrepancies in aerosol forcing assessments, particularly over the absorbing aerosol-cloud overlap regions, i.e., southeastern Atlantic Ocean and South-East Asia (Schulz et al., 2006).

The magnitude and spatiotemporal extent of these effects are driven by several factors, including the magnitudes of the above-cloud aerosol optical depth (ACAOD), the absorption capacity of aerosols (SSA), and properties of underlying clouds (e.g., cloud optical depth), cloud fraction, and spatiotemporal frequency of absorbing aerosols above the cloud. Satellite observations have unambiguously shown the presence of absorbing aerosols above clouds over several regions of the world on a monthly to seasonal scale (Devsthale and Thomas, 2011; Jethva et al., 2018). These regions include the Southeastern Atlantic Ocean and South-East Asia, where massive amounts of biomass burning aerosols are often found to overlie low-level stratocumulus cloud deck from June through September and in March and April, respectively; Tropical Atlantic Ocean, where large-scale dust plumes resulting from outbreaks over the Saharan desert overlie oceanic clouds, and North-East Asia, where dust transported from the Taklimakan and the Gobi deserts possibly mixed with the regional pollution overlies clouds along the eastward transport pathways.

In the past decade, the development of several independent algorithms quantifying aerosol loading above the cloud from satellite-based active and passive sensors has been a major breakthrough. These techniques have shown the potential to retrieve ACAOD using measurements from different A-train sensors, including CALIOP/CALIPSO (Hu et al., 2007; Chand et al., 2008), Aura/OMI (Torres et al., 2012), Aqua/MODIS (Jethva et al., 2013; Meyer et al., 2015), Parasol/POLDER (Waquet et al., 2009). It is imperative for the algorithms designed for the passive sensors to assume the microphysical and optical properties of both aerosols and clouds. The theoretical sensitivity analysis documented in these papers shows that the uncertainty in retrieving ACAOD is primarily governed by the optical properties of aerosols assumed in the inversion. In particular, the assumption of aerosol SSA is known to be the largest source of uncertainty in the inversion. For instance, an uncertain value of aerosol SSA by ±0.03 can result in an error of about +50%/-10% in ACAOD at COD of 10 (Torres et al., 2012; Jethva et al., 2013). The errors in the retrieved ACAOD can be even greater, given the larger perturbation in SSA, especially at higher ACAODs coupled with lower CODs. Peers et al. (2015) demonstrated a method based on the polarized and total radiance measurements of POLDER to show that the radiances at 490 nm and 865 nm can be interpreted as a coupled total and absorption ACAOD given the scattering optical depth of aerosol and their size distribution are known.

In this paper, we introduce a novel algorithm that combines the airborne measurements of the above-cloud AOD and satellite measurements of radiances in the near-UV and visible-near-IR regions of the spectrum to retrieve the SSA and aerosol-corrected COD simultaneously for scenes identified with absorbing aerosols overlaying low-level water clouds. This work builds upon the 'color ratio' (CR) technique previously applied to OMI (Torres et al., 2012; Jethva et al., 2018) and MODIS (Jethva et al., 2013, 2016) sensors. Radiative transfer simulations show that *a priori* information on the ACAOD enables the CR algorithm to retrieve the above-cloud SSA, which otherwise is assumed in the original method.

Section 2 describes the physical basis of the proposed synergy algorithm. The airborne and satellite datasets and their collocation approach are presented in section 3. The optical-microphysical models of aerosols and clouds employed in the algorithm are discussed in section 4. The retrieved spectral single-scattering albedo above clouds and its

110   comparison with equivalent airborne and ground-based measurements/inversions are presented in section 5. The impact of aerosol absorption on the cloud optical depth retrievals is examined in section 6. Expected uncertainties in the retrieved SSA to the input ACAOD and different assumptions made in the algorithm are quantified and discussed in section 7. The concluding remarks and the future application of the proposed algorithm to the CALIOP-OMI-MODIS synergy are presented in section 8.

115   **2   PHYSICAL BASIS**

Light-absorbing carbonaceous particles generated from the biomass burning activities and windblown mineral dust aerosols exhibit a strong wavelength dependence in the UV to visible (VIS) to the shortwave-infrared region (SWIR) (Kirchstetter et al., 2004; Russell et al., 2010). On the other hand, the water clouds exhibit near-neutral wavelength

120   dependence of extinction in this part of the spectrum. Therefore, when absorbing media with strong wavelength-dependent absorption characteristics lie above the clouds, the net effect observed from space is likely to show a stronger spectral signature than what would be expected from just the clouds alone. In other words, this kind of situation produces a strong 'color ratio' effect, which can be seen in the TOA measurements made by satellite sensors such as OMI (Torres et al., 2012) and MODIS (Jethva et al., 2013).

125   The CR method initially developed and applied to the OMI's near-UV observations retrieves ACAOD and COD simultaneously under an assumed state of the atmosphere. The inversion method physically relies on an unambiguous color ratio effect, where the TOA reflectance at shorter wavelengths is lower than that at longer wavelengths, caused by absorbing aerosols having strong wavelength-dependent absorption characteristics when overlaying low-level water clouds. The assumptions involved in the retrieval process include aerosol size distribution, aerosol real and

130   imaginary parts of the refractive index, aerosol vertical profile, and optical-microphysical properties of underlying water clouds. We invoked the radiative transfer (RT) calculations to simulate this effect using a vector discrete ordinate RT model VLIDORT (Spurr, 2006).

Figure 1 shows the simulated reflectance ratio versus single-channel reflectance for the near-UV (354 and 388 nm) and visible wavelength (470 and 860 nm) domains for an atmosphere in which carbonaceous aerosols are assumed to

135   overlay a low-level cloud deck. The particle size distribution (PSD) and spectral properties of aerosols are taken from the long-term direct and almucantar measurements (Version 3, Level 2) made by the Aerosol Robotic Network (AERONET) sunphotometer at *Mongu* (15.25˚S, 23.15˚E), Zambia in central/southern Africa. The vertical profile of aerosols was assumed to follow a quasi-Gaussian distribution with maximum concentration at 3.0 km with an underlying cloud deck of 500-m depth placed between 1.0 and 1.5 km; both are generally consistent with the vertical

140   feature mask produced by CALIOP over the Southeastern Atlantic Ocean. Each dot in Figure 1 represents RT simulation for a specific pair of imaginary part of the refractive index and COD corresponding to a single pair reflectance and color ratio between shorter and longer wavelengths. The presence of absorbing aerosols above the cloud produces a significant reduction in the reflectance and color ratio. For a given AOD, the slope of the solid line depends on both the imaginary index of the lofted aerosol layer above the cloud and COD of the cloud layer underneath

145   the aerosol layer. Thus, for a given value of AOD, TOA measurements from OMI and MODIS at the respective

wavelength pairs can be directly associated with a pair of the imaginary part of the refractive index, which can also be expressed as SSA, and COD. This forms the basis of the proposed above-cloud aerosol retrieval.

3 DATASETS

3.1 AIRBORNE MEASUREMENTS

ORACLES (ObseRvations of Aerosols above CLouds and their intEractionS) was a five-year NASA EVS-2 (Earth Venture Suborbital-2) airborne campaign conducted over the southeastern Atlantic Ocean and off the western coast of central/southern Africa with three Intensive Observation Periods during the biomass burning seasons of 2016, 2017, and 2018. The investigation was designed to acquire high-quality, in situ, and remote sensing measurements of aerosols and clouds for studying key atmospheric processes that determine the climate impacts of the aerosol-cloud system. A detailed overview of the ORACLES campaign, scientific objectives, and instrumentation is presented in Redemann et al. (2021).

Of the various aerosol-cloud measurements acquired during ORACLES, the datasets directly relevant and used in the present work are the direct measurements of spectral aerosol optical depth over clouds from the airborne HSRL-2 lidar and 4STAR sunphotometer. Additionally, we also use the in-situ, inlet-based measurements of spectral SSA acquired from the HiGEAR sensors for the relative comparison against the satellite-based SSA retrievals from OMI and MODIS. In the following sub-sections, we provide a brief description of both datasets.

3.1.1 High-spectral Resolution Lidar-2 (HSRL-2)

The HSRL-2 lidar developed at NASA Langley makes detailed vertical measurements of aerosol backscatter and depolarization (355, 532, 1064 nm) and extinction at 355 nm and 532 nm wavelengths via the HSRL technique to characterize aerosols and clouds. The HSRL technique takes advantage of the spectral distribution of the lidar return signal to distinguish aerosol and molecular signals and thereby measure aerosol extinction and backscatter independently, without a priori assumptions on the aerosol type and/or aerosol extinction-to-backscatter ratio.

HSRL2 flew onboard NASA's ER-2 aircraft during ORACLES-1 and P3-Orion aircraft during ORALCES-2, and -3 deployments, making a total of 7, 15, and 15 flights, respectively, providing direct measurements of the above-cloud column AOD over the southeastern Atlantic Ocean. Additional details describing the HSRL-2 aerosol measurements are given by Burton et al. (2018), and those acquired during the ORACLES mission are provided by Harshvardhan et al. (2022).

3.1.2 Spectrometer for Sky-Scanning, Sun-Tracking Atmospheric Research (4STAR)

The 4STAR is an advanced, next-generation spectrometer developed at the NASA Ames Research Center by the Sunphotometer/Satellite team (Dunagan et al., 2013; Shinozuka et al., 2013; Segal-Rosenheimer et al., 2014; Pistone et al., 2019, LeBlanc et al., 2020), in collaboration with Battelle, Pacific Northwest Division. The 4STAR sensor, in addition to measuring spectral measurements of AOD above the platform in the range 350 nm to 1700 nm, extends the capabilities of the previously developed AATS sensor by adding a sky-scanning mechanism that enables the

retrieval of complex refractive index, shape, and aerosol size distribution. 4STAR can also make measurements of column trace gases (e.g., NO_2) to enhance the accuracy of aerosol measurements via improved aerosol-gas separation. The 4STAR instrument has been integrated onboard multiple airborne research vessels during different field campaigns, including TCAP during 2012 and 2013, SEAC4RS field experiment based out of Huston, Texas in 2013, Arctic field campaign, ARISE, based out of Fairbanks, Alaska in 2014, NAAMES field mission, based out of St-John's Newfoundland, Canada in 2015, and KORUS-AQ based in South Korea in 2016.

4STAR onboard NASA's P3-Orion aircraft flew over the southeastern Atlantic Ocean during all three ORACLES deployments (September 2016, August 2017, and October 2018), and acquired accurate measurements of spectral AODs of biomass burning aerosols in the region, both in cloud-free and above-cloud aerosols areas. The spectral AODs measured from the direct Sun measurements above the clouds, owing to their higher accuracy, constitute a valuable dataset not just to validate the satellite retrievals of ACAOD but to retrieve SSA when combined with the satellite radiance measurements, as demonstrated in the present work.

In addition to making direct measurements of spectral AODs from UV to near-Infrared wavelengths, 4STAR also performed sky scans under favorable flying conditions in either the principal plane or almucantar. The acquired spectral diffuse radiance measurements were processed using a modified, version 2 AERONET retrieval algorithm described in Dubovik and King (2000). The AERONET-like inversion algorithm provided aerosol size distributions, refractive indices, SSA, and AAOD, among other parameters. Out of a total of 174 sky scans in ORACLES in 2016, 38 % (66) met the quality-control (QC) criteria adapted from the AERONET QC available at https://aeronet.gsfc.nasa.gov/new_web/PDF/AERONETcriteria_final1.pdf, which are also listed in Pistone et al. (2019). Of particular interest to the present work, we used 4STAR sky scan-derived spectral SSAs at wavelengths 400 nm, 500 nm, and 660 nm for the comparison against satellite-derived above-cloud SSA from OMI (388 nm) and MODIS (470 nm). The uncertainties in the 4STAR-retrieved spectral SSAs are discussed later in section 5.5, in which the intercomparison of retrieved SSA from the present work against those derived from other ground and airborne sensors is presented.

3.1.3 HiGEAR PSAP and Nephelometer In Situ Observations of Aerosol Scattering and Absorption

During the ORACLES field campaign, aerosol absorption and scattering properties were also measured in situ by PSAP (470, 530, 660 nm) and TSI 3-wavelengths nephelometer (450, 550, and 700 nm) of the Hawaii Group for Environmental Research or HiGEAR, both onboard P3 aircraft. Additionally, two single-wavelength nephelometers (at 550 nm, Radiance Research) were also operated simultaneously to study the increase in light scattering as a function of relative humidity (RH). The PSAP was not controlled in terms of RH; however, its optical block was heated to approximately 50°C in 2016 and 30°C in 2017 to maintain RH within the nephelometer lower than 40%, thereby reducing the artifacts due to changing RH. We adopted the following steps, as suggested by the HiGEAR team, for selecting the optimum values of in-situ spectral SSA.

215   1. The PSAP absorption coefficients were averaged using measurements from the front and rear ends of the instrument to increase the number of input data points.

        2. Consider measurements when the carbon monoxide (CO) measurements from COMA on board P3 and scattering coefficients from TSI sensor are greater than the respective median values obtained from all three campaigns combined, i.e., CO of 142 ppbv, TSI scattering coefficient of 45 mm^{-1}, 36 mm^{-1}, and 27 mm^{-1}, at

220   470 nm, 530 nm, and 660 nm, respectively.

        3. Calculate spectral SSA via TSI_Scat/(TSI_Scat + PSAP_Abs) at 470, 530, and 660 nm.

Furthermore, we apply 100 points temporal averaging to the high-frequency SSA measurements to reduce the noise and variability associated with the measurements. The filtered, temporally averaged spectral SSA dataset from the HiGEAR PSAP/Nephelometer is used in this study for the relative comparison against the satellite-based inversion of

225   SSA above the clouds. The aerosol datasets collected by HSRL-2, 4STAR, and HiGEAR teams for all three years of ORACLES field deployments were accessed from the NASA ESPO archive web portal at the URL https://espoarchive.nasa.gov/archive/browse/oracles.

3.2   SATELLITE OBSERVATIONS

3.2.1   Ozone Monitoring Instrument (OMI)

230   OMI is a hyperspectral radiometer launched on NASA's Aura satellite in 2004, making measurements of reflected light from the Earth in the spectral range of 270-500 nm to retrieve information on trace gases and aerosols (Torres et al., 2007). With a spectral resolution of 0.45-1.0 nm FWHM and instantaneous field-of-view of 3 km binned to 13x24 km^2 spatial resolution at nadir, OMI observes the entire globe daily with an orbital swath width of 2600 km at ground (Levelt et al., 2006). Post-2007, the OMI observations have been affected by a likely external obstruction that perturbs

235   both the measured solar flux and Earth radiance. This obstruction affecting the quality of radiance at all wavelengths for a particular viewing direction is referred to as "row anomaly" (RA) since the viewing geometry is associated with the row numbers on the charge-coupled device detectors. The RA issue was detected first time in mid-2007 with a couple of rows, which over the period of operation, expanded to other rows in 2008 and later. At present, about half of the total 60 rows across the track are identified and flagged as row anomaly affected positions for which no physical

240   retrievals   are   performed.   The   details   about   this   issue   can   be   found   at http://www.knmi.nl/omi/research/product/rowanomaly-background.php. This has significantly affected the sampling during post-2008 OMI measurements, where about half of the OMI swath is blanketed by row anomaly flags. As a result, the spatial coverage is reduced to about half starting in 2009 compared to earlier OMI measurements.

For the present work, the TOA reflectance measurements at 354 nm and 388 nm wavelengths were extracted from the

245   OMI above-cloud aerosol product—OMACA (Jethva et al., 2018). The proposed inversion algorithm was applied to OMI pixels identified with partially absorbing aerosols lofted above clouds following a scheme adopted in the OMACA algorithm (quality flags '0', '1', and '2').

3.2.2 Moderate Resolution Imaging Spectroradiometer (MODIS)

The MODIS sensor launched onboard Terra in 1999 and Aqua in 2002 measure light reflected from Earth in a total of
250 36 spectral bands spanning the shortwave visible to the infrared region of the spectrum. The TOA reflectances measured in these bands at spatial resolutions of 250 m (band 1-2), 500 m (band 3-7), and 1000 m (band 8-36) are used to retrieve a variety of land, ocean, and atmospheric parameters. In the present application, the MODIS Level 1b spectral reflectance data in the 470 nm (band 3) and 860 nm (band 2) wavelength bands and associated observed geometry at a 1-km spatial resolution were averaged over each successive 5 x 5 pixel grid box (~5 x 5 km^2 at nadir).
255 The averaging was performed over pixels identified as liquid water clouds with confident retrieval of COD>3 extracted from the MODIS 1-km cloud optical depth dataset (MOD/MYD06_L2) (Platnick et al., 2017).

Table 1 summarizes the datasets and characteristics of airborne and satellite sensors employed in this study.

3.3 SATELLITE-AIRBORNE SENSORS COLLOCATION

3.3.1 Spatiotemporal Matching

260 Unlike sensors installed on a stationary ground station, the airborne sensor flies on a moving platform both in horizontal and vertical dimensions requiring continuous tracking for spatially collocating with nearby satellite measurements. During ORACLES-1 operation in late August and most part of September of 2016, the HSRL-2 lidar flew onboard the ER-2 platform at a nearly constant altitude of ~20 km, whereas the 4STAR sunphotometer was installed on P3-Orion aircraft sampling the airmass at various altitudes from near-surface to above 6 km along the
265 aircraft trajectory. Both airborne sensors during the ORACLES-2 phase in August and September of 2017 flew on the P3-Orion aircraft, profiling the atmosphere between near-surface to above 6 km.

The OMPIXCOR product of OMI provides ground pixel corner coordinates and associated interception area on the ground corresponding to 75% of the energy in the along-track field of view (Kurosu and Celarier, 2010). Taking advantage of the OMPIXCOR product, the geolocation coordinates of both HSRL-2 and 4STAR were collocated with
270 OMI by identifying airborne measurements that fall within each OMI pixel polygon defined by the OMPIXCOR four corner coordinates within a time difference of ±1 hour between the satellite and airborne observations. The resulting number of observations of ACAOD from the respective airborne sensors was then averaged and assigned to the corresponding OMI pixels for the above-cloud SSA retrievals. One example of OMI-HSRL-2 collocation for the ER-2 flight operated on Sep 24, 2016, is shown in Supplementary Figure 1. The collocation of MODIS TOA observations
275 with airborne measurements was done by averaging both datasets in each regular grid box of size 0.25° x 0.25° within the time difference of ±1 hour.

3.3.2 Adjustment in 4STAR ACAOD

Spectral AOD measurements from the 4STAR onboard the P3-Orion aircraft correspond to an atmospheric column above the aircraft altitude. The P3 aircraft during all three years of ORACLES campaign profiled the atmosphere
280 between the surface to ~6 km and made a limited number of measurements of AOD when the aircraft flew below the aerosol layer and just above the cloud top. Full utilization of the 4STAR dataset requires an adjustment in the

altitudinal measurements of AOD that extrapolates the AOD measured at different altitudes to the cloud top. Such adjustments were performed on each valid measurement of 4STAR based on a quadratic polynomial between altitude and AOD calculated using good-quality observations made during each flight. Figure 3 displays the altitude vs. AOD

285 polynomial of the three relevant wavelengths (388 nm, 470 nm, 501 nm) for a few select flights operated during the three years of ORACLES. Similar plots for all P3 fights with 4STAR AOD profiles derived for all three years are included in supplementary figures 2, 3, and 4. First, the quadratic polynomial relating altitude and AOD for each flight was derived using all good quality data (qual_flag=0), including those measurements that are flagged as AOD above the cloud (flag_acaod=1), was derived. In the next step, the outlier data points that deviate from the polynomial fit by

290 greater than 15% in AOD were rejected. The altitude vs. AOD polynomials were re-calculated with the remaining smoothly varying data points and are used to adjust the altitude-dependent AOD to the cloud-top as follows.

In the first step, AODs recorded at GPS altitude (AOD_{GPSAlt}) and cloud-top altitude ($AOD_{CldTopAlt}$) are calculated from the quadratic polynomials as,

$$AOD_{GPSAlt} = C0 + C1 * Alt + C2 * GPSAlt^2$$

295
$$AOD_{CldTopAlt} = C0 + C1 * Alt + C2 * CldTopAlt^2$$

Second, the difference between the AODs measured by 4STAR (AOD_{4STAR}) and that calculated from the polynomial is calculated as,

$$\Delta AOD = AOD_{4STAR} - AOD_{GPSAlt}$$

In the last step, the adjusted AOD representing columnar aerosol amounts above the cloud-top ($AOD_{AdjtoCldTop}$) is

300 calculated by adding the difference in AOD (ΔAOD) calculated in the previous step to the AOD calculated at cloud-top ($AOD_{CldTopAlt}$) as,

$$AOD_{AdjtoCldTop} = AOD_{CldTopAlt} + \Delta AOD$$

The information on cloud-top altitude for each collocated 4STAR measurement was obtained from the collocated MODIS standard MOD/MYD06 cloud product. The altitude-dependent AOD measurements adjusted to the cloud-top

305 following the above-described procedure were used as input to the proposed SSA inversion algorithm.

We use all good-quality AOD measurements collected during a particular P3 flight to derive the altitude-AOD polynomial specific to that flight, and therefore, it stands as an averaged representation of the AOD profile over the entire flight track. The actual AOD profile below the aircraft level for an instance of 4STAR measurements might differ from the averaged vertical AOD profile for the entire flight. Any deviation in the actual vertical AOD profile,

310 therefore, may result in erroneous above-cloud columnar AOD calculated from the procedure described above. In section 7, we discuss the resultant error in the retrieved above-cloud aerosol SSA due to various input factors, including input ACAODs. It is to be noted here that no such adjustments were made to the collocated 4STAR ACAOD measurements when the P3 aircraft was flying just above the cloud top and below the aerosol layer, as appropriately flagged in the 4STAR dataset.

4   RETRIEVAL ALGORITHM

The physical basis of the proposed retrieval method discussed in the previous section relies on specific assumptions about the optical and microphysical properties of aerosols and clouds. In this section, we describe each of these assumptions as follows.

4.1   AEROSOL MODEL PROPERTIES

The aerosol optical and microphysical models required to generate look-up-tables (LUTs) of spectral TOA reflectance were derived from the multi-year statistics of the AERONET cloud-free, Level 2, version 3 direct measurements and inversions carried out at *Mongu* (15˚S, 23˚E), Zambia, in southern Africa. Multi-year aerosol measurements taken from July through September, when biomass burning activities are widespread over central/southern Africa (Eck et al., 2013), are considered. The particle size distribution is assumed to follow a bi-modal lognormal distribution with the mean and standard deviation of radius for both fine and coarse modes given by the long-term inversion dataset of AERONET (Holben et al., 1998; Dubovik et al., 2002). Similarly, the real part of the refractive index and the Extinction Ångström Exponent in the visible and near-UV spectral domains were also assumed based on the AERONET inversion and direct measurements datasets, respectively. The LUT nodes in the imaginary index at 388 nm and 470 nm encompass a wide range from very absorbing to fully scattering aerosols. The spectral dependence of the imaginary part of the refractive index in the visible-near-IR wavelength range (470-860 nm) is described by the AERONET dataset, whereas that for the near-UV is taken from the OMI/OMAERUV carbonaceous aerosol model (Jethva and Torres, 2011).

To represent the aerosol profile, we take advantage of the detailed vertical measurements of particulate extinction measured by the HSRL-2 lidar. The extinction-weighted aerosol layer height (ALH) for each collocated set of measurements of HSRL-2 was calculated by weighing the altitude grids with their corresponding extinction measurements. The aerosol vertical profile is assumed to follow a quasi-Gaussian distribution around the mean ALH given by the collocated HSRL-2 extinction measurements. In September 2016, HSRL-2 flew on the ER-2 platform at an altitude of ~20 km, measuring the detailed vertical distribution of aerosol extinction in the entire atmospheric column below 20 km and above the clouds in the lower troposphere. The overall extinction-weighted mean (standard deviation) aerosol layer height for a total of 7 ER-2/HSRL-2 flights was calculated as 3.49 (±0.56) km. In August 2017 and October 2018, HSRL-2 was mounted on P3-Orion aircraft and measured the aerosol profiles below the aircraft level and above the cloud top, resulting in an overall mean aerosol layer height of 2.19 (±0.51) and 2.26 (±0.71), respectively. The overall lower aerosol layer height calculated during the latter two years could be likely due to the missing aerosols above 6 km not measured by HSRL-2.

Such detailed vertical information on aerosol profiles is hard to extract from the altitude-dependent 4STAR AOD dataset or is limited to the times of aircraft profiles. Based on the aerosol layer height statistics obtained from HSRL-2 altitude-resolved measurements, therefore, the retrievals of SSA from the satellite-4STAR collocation data were performed assuming a nominal ALH of 3.0 km above mean sea level. The ocean surface is assumed to be Lambertian

with fixed values of surface albedo of 0.05 and 0.03 in the near-UV (354 and 388 nm) and visible-near-IR region (470-860 nm).

4.2   CLOUD MODEL PROPERTIES

355   The proposed method to retrieve aerosol SSA is designed to perform retrievals over low-level liquid water clouds. Clouds are assumed to follow the standard C1 cloud model with Gamma distribution having an effective radius of 6.0 mm (Deirmendjian, 1969). The real part of the refractive indices at 354-388 nm and 470-860 nm were obtained from Hale and Querry (1973). A homogeneous cloud layer with a geometric thickness of 500 meters is assumed to be located beneath the aerosol layer between 850 hPa and 900 hPa pressure levels. The TOA radiances at the near-UV and visible-near-IR wavelengths were calculated for a total of ten nodes in COD, i.e., 0, 2, 5, 7, 10, 15, 20, 30, 40, and

360   50.

4.3   RADIATIVE TRANSFER CALCULATIONS

The proposed algorithm relies on a look-up-table search to find a pair of above-cloud aerosol SSA and underlying COD that explains the TOA reflectance observations from OMI and MODIS independently. We employ the VLIDORT code (Spurr, 2006) to generate the required LUTs for the carbonaceous aerosol model. The code offers the

365   full linearization ability with the outputs of the Stokes vector for arbitrary viewing geometry and optical depth of aerosols and clouds. The model results have been benchmarked against the results published in the literature, as well as used in the operational ACAOD product of OMI (Jethva et al., 2018), research-level ACAOD retrievals from MODIS (Jethva et al., 2013, 2016), DSCOVR-EPIC (Ahn et al., 2021), and S5p-TROPOMI (Torres et al., 2020). The LUTs are referenced to several nodes in ACAOD, COD, the imaginary part of the refractive index, and Sun-satellite

370   viewing geometries listed in Table 2. The observed spectral reflectance from OMI and MODIS are fitted in the 2D retrieval domain calculated for a measured value of ACAOD given by airborne sensors, such as shown in Figure 1, to derive above-cloud SSA and aerosol-corrected COD simultaneously. A simplified flow chart of the proposed airborne-satellite synergy algorithm is shown in Figure 4.

375   # 5   RESULTS

5.1   ACAOD MEASUREMENTS FROM HSRL-2 AND 4STAR

Figure 2 shows the flight tracks of ER-2 and P3-B color-coded with measurements of ACAOD (500 nm) from HSRL-2 and 4STAR sensors operated during August and September of 2016 (a, c) and 2017 (b, d). Each sub-figure also shows the corresponding histogram of ACAOD. Both sensors measured a range of ACAOD (0.0-1.0), with the

380   majority of observations falling between the range 0.2-0.4. The 4STAR aerosol dataset provides a flag for measurements taken when the aircraft was flying above the cloud deck but below the aerosol layer. These measurements are flagged as total column ACAOD, which are shown in the figure. In the proposed inversion algorithm, we use all 4STAR ACAOD measurements taken between aircraft altitudes 1 km and 4 km and adjusted to the cloud-top following the collocation procedure described in section 3.3. The HSRL-2 lidar measured ACAOD from an aircraft

385   altitude of ~20 km from ER-2 in 2016, whereas it flew onboard P3-Orion in August 2017 and October 2018 and measured ACAOD when the aircraft was flying at an altitude of about 5.6 km (averaged over all flights in 2017 and 2018). It is to be noted here that any aerosol layers located above the P3-Orion aircraft altitude are not measured by the HSRL-2, and therefore, will be missed in the ACAOD measurements, leading to underestimation in columnar aerosol loading in such cases.

390   **5.2   NEAR-UV SSA RETRIEVALS FROM OMI-ORACLES SYNERGY**

The spatial distribution of retrieved above-cloud aerosol SSA at 388 nm wavelength along the flight tracks from OMI-ORACLES synergy is shown in Figure 5. The results derived from OMI-HSRL-2 (OMI-4STAR) are shown in the left (right) panels. Each subplot also displays the corresponding histogram of retrieved SSA at 354 nm (blue) and 388 nm (red). The retrievals of SSA shown in the figure correspond to the collocated airborne ACAOD (500 nm) > 0.2

395   measured from HSRL-2 and 4STAR. Among all four synergies, the OMI-HSRL-2 yields the maximum number of matchups (N=140) during the 2016 campaign due to broader spatial coverage of ACAOD measured from HSRL-2 than was available from 4STAR or from HSRL-2 on P3 in 2017 and 2018. Note that about half of the OMI swath was affected by the row anomaly during the ORACLES operation period, resulting in fewer matchups between valid OMI and airborne observations. The retrieved SSA at UV wavelengths for the majority of the matchups is found in the

400   range of 0.88-0.91, with an ACAOD-weighted value of 0.88 (0.89) at 354 nm (388 nm). A few matchups obtained from the August 2017 and October 2018 campaigns were a result of the limited availability of HSRL-2 ACAOD measurements from P3 aircraft.

The OMI-4STAR synergy yielded a total of 52 matchups in September 2016, with the retrieved SSA at both UV wavelengths to be 0.91-0.92, larger by 0.03 than those obtained from the OMI-HSRL-2 combinations. For the latter

405   two years of ORACLES deployments, i.e., August 2017 and October 2018, OMI-4STAR provides significantly greater matchups than HSRL-2-OMI due to more availability of altitude-dependent AOD measurements, which are adjusted to the cloud top following the procedure described in section 3.3.2. The retrieved above-cloud SSAs at 354 nm and 388 nm were in the range of 0.84-0.92, with the histograms peaking at 0.88 and 0.89 at the respective wavelengths. For the October 2018 deployment, a total of 19 matchups of OMI-4STAR observations yield SSA

410   distribution peaking at 0.92 and 0.93 at UV wavelengths.

5.3   VIS SSA RETRIEVALS FROM MODIS-ORACLES SYNERGY

Figure 6 shows maps of retrieved above-cloud aerosol SSA at 470 nm wavelength from MODIS-ORACLES synergy. A noticeable feature of SSA retrievals in the visible channel is a significant increase in satellite-airborne matchups relative to OMI near-UV retrievals owing to the availability of original higher spatial resolution measurements at 1

415   km re-gridded to 5 x 5 km box at the nadir. Again, the MODIS-HSRL-2 collocation provided maximum retrieval matchups (N=298), followed by those with 4STAR (N=154) for the August 2016 observations. The histogram of the retrieved SSA at 470 nm (blue) from both HSRL-2 and 4STAR synergies shows a range of values between 0.84-0.96 peaking around 0.89 during ORACLES-1 operation (September 2016). For the 860 nm wavelength, the retrieved SSA peaked around 0.83-0.85. For the ORACLES-2 operation (August 2017), the total number of airborne-satellite

420   matchups was significantly lower, yielding ACAOD-weighted SSAs of ~0.86 and ~0.81, at both wavelengths, respectively, which are lower than the SSA values derived from ORACLES-1 observations. The airborne-MODIS synergy resulted in the lowest number of matchups for ORACLES-3 October 2018 deployment due to a limited number of ACAOD (500 nm) measurements greater than 0.2. Both HSRL-2 and 4STAR synergies with MODIS retrieve above-cloud SSAs of 0.90 and 0.85 at 470 nm and 860 nm, respectively, which represent relatively largest

425   values of SSA among all three years of ORACLES measurements.

5.4   DEPENDENCY OF RETRIEVED SSA ON ACAOD

The proposed satellite-airborne synergy algorithm was performed using all airborne ACAOD observations > 0.1 at 500 nm collocated with OMI and MODIS sensors. It is expected that the inversion of SSA and cloud optical depth should be robust at higher values of ACAOD owing to greater sensitivity to TOA reflectance and color ratio, hence

430   better resolved retrieval domain space, as shown in Figure 1. To assess the dependency of the retrieved SSA to the input ACAOD, the retrievals are binned as a function of ACAOD and plotted as a box and whisker plot in Figure 7. The top (bottom) panel shows OMI-retrieved SSA at 388 nm (MODIS-retrieved SSA at 470 nm) as a function of collocated airborne ACAOD measured from HSRL-2 lidar and 4STAR sun photometer combined during all three years of ORACLES. The mean and median values of SSA for each AOD bin size of 0.1 are shown as dots and solid

435   lines, whereas the shaded box contains 50% percentile of data. A noticeable feature in both plots is the tendency of the synergy algorithm to retrieve relatively lower values of SSA at the near-UV and VIS wavelengths for the AOD bin 0.1-0.2. At such lower values of ACAOD, the 2D retrieval domain (not shown in Figure 1) collapses to a very narrow region, i.e., the sensitivity to TOA reflectance and color ratio diminishes significantly. Given the assumptions in the algorithm and their associated uncertainties, it is practically harder to retrieve SSA reliably at lower ACAOD.

440   However, at moderate to larger values of ACAOD, the retrieved SSAs at both wavelengths are largely stable and do not show a well-defined behavior with ACAOD. The variations in the retrieved SSA, shown as shaded boxes and whiskers, therefore, largely attributed to the actual variations in the aerosol absorption within the spatial and temporal domain of ORACLES. This analysis has suggested that the retrieved SSA at much lower ACAOD (~0.1-0.2) at the mid-visible wavelength could be biased low, whereas retrievals are found to be stable at moderate to higher ACAODs

445   (>0.2).

5.5   COMPARISON WITH AERONET GROUND INVERSIONS AND IN-SITU/REMOTE SENSING MEASUREMENTS OF SSA

The satellite-based SSA retrievals in clear-sky conditions as well as above the cloud proposed in this work are hard to validate due to the scarcity of equivalent columnar, in situ measurements of aerosol absorption. Such validation efforts

450   require well-coordinated airborne, full atmospheric column measurements of aerosol absorption properties aligned with satellite overpass time. To evaluate the relative agreement and differences in the retrieved above-cloud aerosol SSA from the present synergy, we used the following three independent datasets of SSA acquired over the southeastern Atlantic Ocean during the ORACLES period: 1) the aerosol SSA dataset derived from absorption and scattering properties measured in situ onboard P3 by PSAP (470, 530, 660 nm) and TSI 3-wavelengths nephelometer (450, 550,

455 and 700 nm) of HiGEAR team, 2) ground-based inversion of spectral SSA from AERONET at an inland Mongu site, and 3) UV-VIS spectral SSA dataset retrieved from the synergy of AERONET-OMI-MODIS at Mongu site from the work of Kayetha et al. (2022).

Figure 8 shows a composite comparison chart of the retrieved spectral SSA above the cloud from the present work and those obtained from the above-mentioned three spectral SSA datasets for the ORACLES-1 (top) and -2 (bottom)
460 campaigns. The above-cloud SSA retrievals from OMI (354 nm, 388 nm) and MODIS (470 nm, 860 nm) are shown as a standard box and whisker (BW) plot format, where the mean and median are presented as filled circles and horizontal lines; shaded boxes (light blue for OMI and orange for MODIS) represent data points contained within 25-75 percentiles; and thin vertical lines as 1.5 times interquartile range (75 minus 25 percentile). The corresponding SSA retrievals shown at the 660 nm wavelength were derived by linearly interpolating SSA between 470 nm and 860 nm.
465 The in situ spectral SSA dataset derived from PSAP+nephelometer measurements for the respective two years of the ORACLES campaign is shown as red-outlined BW at corresponding measurement wavelengths of 470 nm, 530 nm, and 660 nm. Note that these datasets were not spatially and/or temporarily collocated. Instead, the respective datasets collected during the three years of ORACLES were aggregated separately to derive statistics shown in Figure 8.

For the ORACLES operation in September 2016, the above-cloud aerosol SSA at visible wavelengths from MODIS
470 is found to be about 0.02 higher than that measured in situ from PSAP+nephelometer sensors. While both datasets show a comparable spread in the retrieved SSA, the mean and median values of the present above-cloud aerosol SSA are noted ~0.02 higher. Due to the non-availability of in situ measurements of SSA in the near-UV region, no such comparison was made for the OMI-based SSA retrievals at 354 and 388 nm.

The retrieved above-cloud aerosol SSA from OMI and MODIS are also compared against those derived from sky scan
475 observations made by the 4STAR sunphotometer. During the ORACLES-1 September 2016 operation, 4STAR on P3 Orion aircraft made the measurements of diffuse sky radiation at five wavelengths, i.e., 400 nm, 500 nm, 675 nm, 870 nm, and 995 nm. Using an AERONET-like inversion procedure, these sky radiances are inverted to retrieve particle size distribution and the real/imaginary part of the refractive index. The errors in the 4STAR-retrieved SSAs are mainly driven by the uncertainties in the input AOD and sky radiances. The uncertainties in the measured AOD are
480 wavelength-dependent and also vary with the time of measurements and solar zenith angle. These values were typically between 0.01 and 0.02, ranging from a low of 0.008 to a high of 0.037 in an extreme case. On the other hand, uncertainties in radiance measurements are quantified between 1.0 % and 1.2 % for the 470-995 nm spectral range, which is wavelength dependent but constant for the entire 2016 campaign (Pistone et al., 2019).

Figure 9 compares spacetime collocated OMI- and 4STAR-retrieved SSA for the ORACLES-1 September 2016
485 campaign. OMI retrievals of above-cloud SSA were spatially collocated within 1° square box centered at the 4STAR/P3-B geolocation for the days when 4STAR made successful sky scans followed by SSA inversions, as indicated in the legends (bottom-left) with different colors. Each circle in the figure represents a single matchup between the two sensors, where the size of the circle denotes the range of coincident AOD [500 nm] measured by 4STAR. The OMI-4STAR SSA comparison was performed for the two sets of OMI retrievals, i.e., one derived from
490 using the original aerosol model listed in Table 2 and one with the modified aerosol model (see the following

paragraph). The OMI-4STAR matchups are found to be in good agreement within ±0.03 difference for the P3 flights operated on September 12 and 14, for which the corresponding AODs were in the range 0.2-0.4. For other flights, OMI SSAs are noted biased high by ~0.05 relative to the 4STAR inversions. Overall, the comparison yields a root-mean-square-difference of 0.049 and bias of 0.040 with close to 50% (30%) matchups agreeing within ±0.03 (±0.05)

495   difference.

One of the assumptions to which the TOA radiances in the near-UV region are sensitive is the assumed spectral dependence of aerosol absorption or Absorption Ångström Exponent (AAE) both in cloud-free (Jethva and Torres, 2011) and above-cloud aerosols scenes (Jethva et al., 2018). The optical properties assumed in the present near-UV aerosol model are adopted from the standard OMI-OMAERUV cloud-free aerosol algorithm, which has provided a

500   good agreement in both AOD and SSA retrievals with those of ground-based AERONET globally (Ahn et al., 2014; Jethva et al., 2014). However, a departure of the assumed spectral properties from those of actual aerosols may introduce errors in the retrieved above-cloud SSA. For the sake of sensitivity analysis, we modified the original near-UV aerosol model by reducing the relative spectral dependence of the imaginary part of the refractive index from 20% (the original assumption) to 10% between 354-388 nm, resulting in lower AAE of ~1.73-1.87 compared to AAE of

505   ~2.45-2.60 assumed in the original aerosol model. This is achieved by lowering the imaginary part of the refractive index at 354 nm, keeping it the same for the 388 nm wavelength. As shown in Figure 9 (b), the above-cloud SSA retrieved using the modified aerosol model shows relative improvements with reduced RMSD and an increased number of matchups within 0.03 and 0.05 error limits. However, a positive relative bias of ~0.03 still remains.

A similar comparison of the retrieved SSA at 470 nm and 670 nm from MODIS against those of 4STAR inversions is presented in Figure 10. During ORACLES-1 deployment in September 2016, 4STAR took sky measurements and

510   retrieved SSA at 400 nm, 500 nm, 675 nm, 870 nm, and 995 nm wavelengths. To facilitate a direct comparison with satellite retrieval, the 4STAR SSAs were linearly interpolated to the 470 nm wavelength. MODIS 470-nm SSAs compare relatively better with RMSD and bias of 0.034 and 0.024, respectively, where about 52% and 73% of the matchups are found within 0.03 and 0.05 differences, respectively. Both inversions show relatively greater absorption

515   (lower SSA) at 670 nm, generally consistent for the fine mode particles; however, yielding slightly larger RMSD and bias compared to those at 470 nm.

For the ORACLES-2 deployment in August 2017, 4STAR inversion dataset reports SSA at four wavelengths, excluding the shortest 400 nm wavelength due to contamination issues. Therefore, the 4STAR SSAs linearly extrapolated to 470 nm based on the 500-675 nm SSAs. The comparison in Figure 10 (b) shows greater variability in

520   the 4STAR SSAs in the range 0.80-0.95, where 34% (22%) and 53% (42%) of MODIS-retrieved 470 nm (670 nm) SSAs are in agreement within 0.03 and 0.05 limits, respectively. No meaningful relation between the disagreement in SSAs and measured AODs was noticed as several airborne-satellite matchups having both low to moderate and higher aerosol loadings were found to agree well within ±0.03 differences. SSA matchups having disagreements larger than 0.05 are those with 4STAR SSAs in the range 0.86-0.94 but MODIS-retrieved SSAs still lower than 0.86 at both 470

525   nm and 670 nm wavelengths. Several factors, including spatiotemporal mismatch, columnar (satellite) vs. above-

aircraft (4STAR) representation of SSAs, and inherent uncertainties in both inversion techniques, could be attributed to the observed discrepancies, which need further investigation.

6   IMPACT OF AEROSOL ATTENUATION ON CLOUD OPTICAL DEPTH RETRIEVALS

The lofted layers of absorbing aerosols over the clouds attenuate light reflected by the cloud top through scattering and absorption. This effect reduces cloud-reflected upwelling UV (Torres et al., 2012) and VIS-NIR radiation (Jethva et al., 2013; Meyer et al., 2015), reaching the TOA and measured by the satellite sensors. Therefore, retrievals of COD derived from passive sensors such as OMI and MODIS in the UV to VNIR spectrum are expected to be biased low if absorbing aerosols are not accounted for in the inversion. The magnitudes of bias in the apparent COD depend on the strength of aerosol absorption and backscattering as well as on the actual value of COD (Jethva et al., 2018). The proposed satellite-airborne synergy algorithm retrieves two sets of COD, one corrected for the presence of absorbing aerosols overlying the cloud deck, and one retrieved assuming no aerosols above the cloud, which is termed as the apparent COD. Comparing these two sets of CODs is worthwhile to estimate the bias in COD retrievals due to the presence of aerosols above clouds.

Figure 11 (a) shows a comparison of the aerosol-corrected COD (y-axis) to the apparent COD (x-axis) retrieved from both OMI and MODIS observations at 388 nm (red) and 860 nm (blue), respectively. The synergy retrievals from HSRL-2 and 4STAR ACAOD (>0.2 at 500 nm) datasets acquired during ORACLES 2016 and 2017 campaigns were used here. The aerosol-corrected CODs are found to be higher compared to apparent CODs (not corrected for aerosols) by an average (standard deviation) value of 16.33% (±17.10%) and 7.53% (±7.99%) at 388 nm and 860 nm, respectively. In other words, if not accounted for the presence of absorbing aerosols above the clouds, the retrieved COD turns out to be about -12.16% (±13.15%) and -6.52% (±6.60%) biased low compared to the aerosol-corrected CODs at UV and NIR wavelengths, respectively. The linear regression fits show a negative intercept of ~1, pointing to the inherent uncertainties involved in the proposed inversion technique at lower COD values.

Figure 11 (b) and (c) further parameterize the same data group and present the % difference in COD, i.e., aerosol-corrected minus apparent (non-corrected), as a function of above-cloud aerosol absorption AOD (AAOD) at 388 nm of OMI and 470 nm of MODIS, respectively. Each colored box represents 25 to 75-percentile data grouped in an AAOD bin size of 0.01. Different colors denote data group corresponding to different ranges of CODs. At both UV and NIR wavelengths, the magnitudes of % difference in COD have strongly correlated with and turn out to be a bifunction of AAOD as well as the actual values of CODs. The differences between the aerosol-corrected and non-corrected COD not just increase with increasing aerosol absorption above clouds (AAOD) but are also enhanced by larger COD underneath the aerosol layer. For instance, at a given value of AAOD, the differences between the aerosol-corrected and non-corrected CODs are found to be larger at higher CODs. These results are significant and further signify the importance of aerosol absorption above clouds in the UV to VIS-NIR spectral region in at least two ways. First, aerosol absorption above clouds, if not accounted for in the remote sensing inversion, can potentially introduce a negative bias in the retrieved cloud optical depth retrieval, whose magnitude depends on the strength of aerosol absorption (AAOD) and cloud brightness (COD) underneath the aerosol layer. Second, an accurate estimate of the radiative effects of aerosols above the cloud requires the true COD at the cloud-top along with AAOD.

7   POSSIBLE SOURCES OF UNCERTAINTIES

When synergized with satellite observations, the direct measurements of ACAOD from airborne sensors allow for retrieving above-cloud aerosol SSA (see Figure 1). The accuracy of retrieved SSA, therefore, is primarily governed

565   by, in addition to the other algorithmic assumptions, the accuracy of measured ACAOD and its spatiotemporal collocation with satellite observations used as input to the inversion algorithm. Additionally, the imperfectness in collocating airborne and satellite datasets may introduce a mismatch between observed AOD conditions and corresponding reflectance from the satellite. For instance, AODs from airborne sensors are columnar point measurements, whereas satellite observations correspond to the pixel area projected on the ground. Furthermore, the

570   limited availability of airborne measurements in the given pixel polygons (OMPIXCOR coordinates product for OMI and 0.25 deg. grid box for MODIS) may not fully represent the atmospheric conditions observed by the satellite sensor in the pixel area or chosen spatial windows.

7.1   ERROR IN SSA DUE TO UNCERTAIN ACAOD

To quantify the error in the retrieved SSA due to the uncertainty in the input ACAOD, we adopt a perturbation-based

575   approach, in which the observed ACAOD was perturbed in both directions, i.e., underestimation and overestimation. The resultant retrievals of SSA were compared against those obtained from the original set of input ACAODs. The direct measurements of columnar ACAOD above the cloud deck do not require adjusting the measurement to the cloud-top, such as performed on the 4STAR ACAOD data, thereby reducing the uncertainty in the input ACAOD to the synergy algorithm. For this reason, we select the collocated HSRL-2 and OMI/MODIS datasets of the ORACLES-

580   1 campaign to perform the SSA uncertainty analysis. The retrievals of above-cloud SSA were performed with the perturbed airborne ACAODs in the range -40% to +40% in step of 10%. The retrieved SSA in each step of the perturbation was compared against the original SSA derived from the unperturbed ACAODs to calculate the corresponding errors in the SSA.

The error matrix in the derived above-cloud SSA from the described procedure is shown in Figure 12 as well as

585   tabulated in Tables 3 and 4 for the 388 nm and 470 nm wavelengths, respectively. For the OMI-based near-UV SSA retrievals, an error of -40% (underestimation) in ACAOD results in an absolute error of -0.05 in the retrieved SSA, the magnitude of which decreases to about -0.02 and -0.01 given the ACAOD perturbation of -20% and -10%, respectively. On the other hand, overestimated ACAOD yields a much lesser error of +0.002, +0.005, and +0.01 in SSA following the ACAOD perturbation of +10%, +20%, and +40%, respectively. The SSA retrievals in the visible

590   domain (470 nm) also responded to the perturbation in ACAOD but with significantly reduced sensitivity resulting in an error in SSA of ~-0.02, -0.006, and -0.003 given the ACAOD uncertainty of -40%, -20%, and -10%; the errors in SSA were +0.01, +0.005, and +0.002 when ACAOD was overestimated in the same proportion. The larger sensitivity of SSA to the ACAOD in the near-UV domain reflects the spectral dependence of extinction produced by fine-mode carbonaceous aerosols, resulting in relatively higher (lower) AODs at shorter (longer) wavelengths, thereby producing

595   a larger absolute change in ACAOD given fixed perturbation. Since ACAOD for fine mode smoke particles are higher at shorter wavelengths, perturbing ACAODs by, say, 20% at 388 nm would produce a larger absolute difference in ACAOD than that caused by the same perturbation (20%) in ACAOD at 470 nm.

The ACAOD measurements from airborne HSRL-2 are accurate within the absolute uncertainty of ~0.01-0.02, which is equivalent to that of the ground-based AERONET data. For the September 2016 operation of ORACLES, the HSRL-2 data of the R9 version reports the absolute uncertainty in ACAOD measurements at 355 and 532 nm, which for the former wavelength was in the range of 0.8%-1.8%. Such uncertainty estimates for the remaining two years of HSRL-2 operation in 2017 and 2018 are not yet available. Assuming similar levels of uncertainty during all three years of HSRL-2 operation, an error of 2% in the measured ACAOD would produce an error of ±0.002 in the retrieved SSA at 388 nm and 470 nm. The 4STAR dataset of altitude-dependent AOD collected during all three years of the ORACLES campaign provides absolute uncertainty for each instance of AOD measurement. The overall uncertainty in the 4STAR AOD measurements (>0.2 at 500 nm) collocated with OMI and MODIS was in the range of 1%-18% with mean values of 4.3% and 4.8%, respectively. An additional source of uncertainty in using the 4STAR AOD is the vertical adjustment of altitude-dependent AODs to the observed cloud top. While we use actual AOD values measured at the corresponding altitudes adjusted to the cloud top using an averaged AOD profile derived for a specific flight (i.e., Figure 3), any departure of the actual profile from the averaged profile would yield erroneous AODs at the cloud top. The magnitude of error in vertically adjusted AODs depends on the variability of aerosol vertical distribution in spatial areas covered by the aircraft. It is hard to quantify this part of the error in AOD due to the lack of vertically resolved aerosol measurements along the P3/4STAR tracks. Assuming an overall 10% error in the measured AOD, including absolute error in the measurements, imperfectness in spatial-temporal collocation, and non-representativeness averaged AOD profile, would result in an error of less than 0.01 in the retrieved SSA at both wavelengths.

7.2 ERROR IN SSA DUE TO UNCERTAIN AEROSOL LAYER HEIGHT

The proposed synergy algorithm also involves an assumption of the aerosol vertical profile and mean layer height above the cloud deck. In the SSA inversion, the detailed vertical distribution of extinction measured by HSRL-2 for each collocated measurement was used to calculate the extinction-weighted mean aerosol layer height and assigned to the corresponding OMI/MODIS retrieval instances. The 4STAR sensor does not provide detailed, full-column vertical measurements of aerosols. Therefore, in the absence of such information for 4STAR-satellite collocated measurements, the algorithm relied on the ALH database adopted in the OMI standard OMAERUV aerosol algorithm. The OMI ALH dataset derived from the 30-month long collocated OMI-CALIOP measurements in clear-sky conditions (Torres et al., 2013) is expected to be accurate within ±1 km. The corresponding errors in the present above-cloud SSA retrieval obtained following the perturbation approach are found to be relatively lower, where an underestimated (overestimated) ALH by 1 km produces an error of -0.008 (-0.005) and -0.005 (negligible) at 388 nm and 470 nm wavelengths, respectively. Relatively larger errors in the retrieved SSA at near-UV wavelength signify the radiative interactions between the molecular Rayleigh scattering and aerosols-clouds, which gradually decrease at longer wavelengths, thereby producing lesser errors in the retrieved SSA at longer wavelengths.

7.3 ERROR IN SSA DUE TO UNCERTAIN ABSORPTION ÅNGSTRÖM EXPONENT (AAE)

Another important parameter that can affect the accuracy of the retrieved SSA is the value of Absorption Ångström Exponent (AAE) assumed in the aerosol model for both near-UV and VIS domains. AAE describes the spectral

dependence of aerosol absorption and contributes to the 'color ratio' effect at TOA in addition to the magnitude of
AOD and brightness of the cloud or COD. For instance, explaining two-channel TOA reflectance observations
assuming two distinct values of AAE result in different AOD retrievals in clear-sky (Jethva and Torres, 2011) as well
as in the above-cloud aerosol situation (Jethva et al., 2018). The AAE for the near-UV aerosol model used in the
present study was adopted from the standard OMI/OMAERUV carbonaceous aerosol models based on above two
studies. A strong relative spectral dependence of 20% in the imaginary part of the refractive index between 354 nm
and 388 nm, resulting in AAE of 2.45-2.60 (see Table 2), is expected to adequately represent the organic content of
the carbonaceous smoke from biomass burning.

More recently, Kayetha et al. (2022) retrieved spectral SSA following the synergy between ground-based AOD and
OMI-MODIS observations for the clear-sky scenes over more than 100 AERONET sites. The retrieved AAE values
in the near-UV (354-388 nm) and visible domains (470-660 nm) over *Mongu* station in central/southern Africa
representing biomass burning fine mode smoke particles were retrieved as 2.49 (3.02) and 0.92 (0.81), respectively,
for the Jun-Jul-Aug (Sep-Oct-Nov) season. The corresponding spectral dependence in the retrieved imaginary part of
the refractive index at the near-UV wavelengths was noted ~ 13% and 20% for JJA and SON seasons. The AAE values
(1.15-1.35) for the visible wavelength range (470-860 nm) are directly adopted from the ground-based AERONET
inversion database.

For estimating errors in the retrieved SSA due to change in the assumed AAE, the imaginary part of the refractive
index at 354 nm and 860 nm was perturbed by ±10%, while retaining the original values at 388 nm and 470 nm as
described in the aerosol model (Table 2). The corresponding change in AAE in the near-UV and visible wavelength
domains were noted ±0.7 and ±0.12, respectively. An increase (decrease) in the imaginary index at shorter wavelength
results in steeper (reduced) spectral dependence of aerosol absorption or AAE. The above-cloud aerosol LUTs were
re-generated by performing RT calculations with a perturbed imaginary part of the refractive index. Other input
parameters were unchanged and kept the same as described in the original aerosol model. The above-cloud SSA was
retrieved using the perturbed aerosol LUT and compared against the original retrieval dataset derived from the
OMI/MODIS-HSRL-2 synergy. For the near-UV domain, we find that changing the imaginary part of the refractive
index at 354 nm by +10% (-10%) or AAE by +0.67 (-0.73), produces an error in the retrieved SSA by +0.02 (-0.029).
In other words, an increment (decrement) in the assumed AAE value yields overestimation (underestimation) in the
retrieved SSA above the clouds. Similar results were found for the visible domain (470-860 nm), albeit with much
lower magnitudes of error in SSA (+0.004, -0.005) resulting from the corresponding change in AAE. Larger errors in
the retrieved SSA at 388 nm compared to those at 470 nm signify the greater sensitivity of TOA radiance to the aerosol
absorption above the cloud in the near-UV region.

7.4 ERROR IN SSA DUE TO PARTICLE SIZE DISTRIBUTION AND REAL PART OF REFRACTIVE INDEX
Finally, the errors in the retrieved SSA were quantified due to changes in the assumed aerosol particle size distribution.
The aerosol model used in the present work was essentially developed using long-term AERONET direct and
inversion measurements collected at the Mongu site in Zambia (Table 2), which is located in the center of biomass
burning activities in central/southern Africa. Although we assume that the aerosol PSD model adequately represents

670   the transported carbonaceous smoke above clouds over the Atlantic Ocean, the sensitivity of the retrieved spectral SSA to changes in the actual PSD from the assumed one, therefore, should be quantified. The sensitivity of the retrieved spectral SSA is quantified by comparing the original retrieval dataset of 2016 OMI-MODIS-HSRL-2 synergy against the new dataset retrieved using the perturbed aerosol PSD models with +/- 20% and +/-5% perturbations in fine mode radius and real part of the refractive index, respectively. The resultant difference in the retrieved SSA at

675   388 nm and 470 nm are included in Table 3 and Table 4, respectively.

An underestimation in the fine mode radius by 20%, i.e., from 0.0898 μm to 0.07184 μm (0.10776 μm), produces errors in SSA mostly lesser than +0.005 at both 388 nm and 470 nm. On the other hand, an overestimated fine mode radius by 20% produces errors in SSA up to +0.03 with a mean value of +0.022 at 470 nm, whereas the error in SSA was noted lower than +0.01 at 388 nm. Similarly, an underestimation (overestimation) in the real part of the refractive

680   index by 5% results in a mean error in SSA of +0.01 (-0.015) at 388 nm and +0.03 (-0.01) at 470 nm. Noticeably, a perturbation in the real part of the refractive index around its original value yields error in SSA in a symmetrical way, i.e., an underestimation and overestimation produce positive and negative errors, albeit the magnitude of errors is different, where overestimation in the real part of the refractive index results in larger positive errors.

7.5   ERROR IN SSA DUE TO NOT ACCOUNTING FOR NO2

685   In the present inversion of above-cloud SSA, the trace gases were not accounted for explicitly, except that the columnar Ozone (O_3) amount was kept at a constant value of 275 Dobson Unit (DU) in the RT simulations for creating aerosol-cloud LUT. In addition to the spectral AODs above aircraft, 4STAR also measured the vertical column densities (VCD) of trace gases such as Ozone (O_3), and NO_2. The mean/median of vertical column densities (VCD) of O_3 measured by 4STAR onboard P3 for the September 2016 and August 2017 deployments were ~335 DU and

690   ~267 DU, with a standard deviation of ~27 DU and ~13 DU, respectively. The assumed constant value of O3 of 275 DU in the aerosol-cloud LUT is quite closer to the mean amount measured by 4STAR in August 2017, but lower by 60 DU for September 2016. Since the wavelengths of the SSA retrieval from OMI (354 nm and 388 nm) and MODIS (470 nm and 860 nm) are known to be mostly unaffected by the O_3 absorption, we don't expect any significant error in the retrieved above-cloud SSA due to changes in the O_3 amounts.

695   To quantify the error in the retrieved SSA due to unaccounted NO_2, additional LUTs were generated assuming columnar NO_2 amounts of 0.25 DU and 0.50 DU embedded with aerosols and cloud parameters tabulated in Table 2. The retrievals of above-cloud SSA were performed using these new LUTs and compared against the original OMI-HSRL-2 synergy inversion dataset to calculate the corresponding error in SSA caused by changing NO_2 amounts. We find that accounting for the presence of NO_2 by amounts 0.25 DU, and 0.5 DU produces differences in the retrieved

700   above-cloud SSA at OMI wavelength of 388 nm by -0.004 (±0.004), -0.007 (±0.007), and -0.017 (±0.011), respectively. In other words, not accounting for the columnar NO_2 absorption effects, the retrieved SSA at 388 nm are subjected to an overestimation by the stated quantities given respective change in the columnar NO_2 amounts. For the blue band of 470 nm of MODIS, the retrieved SSAs by adding NO_2 amounts of 0.25 DU and 0.50 DU in the inversion are found to be higher by 0.006 and 0.011, respectively.

705   The columnar NO$_2$ amounts commonly retrieved from Aura-OMI and Sentinel5p-TROPOMI sensors over the biomass burning regions of continental central/southern Africa ranges from 2-10 (x10^{15} molecules/cm^2) or 0.07 DU to 0.37 DU (https://so2.gsfc.nasa.gov/no2/pix/regionals/Africa/Africa.html). However, due to its shorter lifetime and along the westward transport pathways of smoke, the NO$_2$ VCD amounts over the ocean reduced significantly to 2-5 (x10^{15} molecules/cm^2) or 0.07 DU to 0.19 DU (personnel communication: Lok Lamsal—NO$_2$ remote sensing expert at NASA

710   Goddard Space Flight Center). Given such lower columnar amounts of NO$_2$ (<0.2 DU) over the ocean, the expected errors in the retrieved SSA above clouds are up to ~0.005 or lower.

8   SUMMARY AND FUTURE IMPLICATIONS

The 'color ratio' method designed to quantify aerosol loading above clouds using the TOA reflectance measurements from OMI and MODIS in the near-UV and VIS-NIR domains, respectively, assumes an aerosol model involving

715   intrinsic optical properties of scattering and absorption. The theoretical RT simulations of aerosols above clouds showed an unambiguous, distinct sensitivity to the three main radiatively important parameters of aerosol-cloud overlap scene, i.e., ACAOD, COD, and SSA. Earlier studies noticed a marked sensitivity of the retrieved ACAOD from UV and VIS passive sensors to the assumed imaginary part of the refractive index or SSA. For instance, Jethva et al. (2018), through theoretical simulations, quantified that an error of ±0.03 in the assumed aerosol SSA above the

720   cloud can produce uncertainty in the retrieved ACAOD at 388 nm in the range -20% to -24% and 42%-46% under an underestimated and overestimated SSA scenarios, respectively. Similarly, the errors in the retrieved ACAOD at 500 nm were estimated to be from -10% to +46% to the perturbation of ±0.03 in the assumed SSA. Both studies showed that the sensitivity of the retrieved ACAOD to the change in SSA follows a dynamic behavior that depends on the magnitudes of both ACAOD and COD.

725   The RT simulations demonstrate that the availability of ACAOD from an external source, when constrained in the color ratio algorithm, allows the retrieval of the imaginary part of the refractive index of the lofted aerosol layer and the optical depth of the cloud underneath simultaneously. The availability of high-quality, direct ACAOD measurements from airborne sensors HSRL-2 lidar and 4STAR sunphotometer acquired during the ORACLES campaign for 2016, 2017, and 2018 conducted over the southeastern Atlantic Ocean offered an unprecedented

730   opportunity to test the proposed algorithm. The aerosol particle size distribution, the real part of the refractive index, and the spectral dependence of aerosol absorption required to build the aerosol model were adopted from the long-term AERONET inversion data collected at the Mongu site in Zambia for the VIS-NIR domain, whereas the latter was based on the standard OMI-OMAERUV operational algorithm for the near-UV domain. The multidimensional aerosol-cloud LUT was derived using the VLIDORT radiative transfer model accounting for a wide variety of aerosol

735   loading, cloud brightness, and Sun-satellite geometry. The spacetime collocated data of HSRL-2/4STAR ACAOD and TOA spectral radiances from OMI and MODIS were processed with the synergy algorithm.

The retrieved above-cloud aerosol SSA at the near-UV (388 nm) and VIS (470 nm) wavelengths showed relatively lower bias with large variability (~0.8-0.95) at lower ACAOD (<0.2), above which the retrievals were more stable, rendering no meaningful relation ACAOD for moderate to larger aerosol loadings. Under the lower aerosol loading

740   conditions, the uncertainties in the assumed aerosol-cloud properties appear to dominate over the above-cloud aerosol
        signal resulting in larger variabilities in the retrieved SSA.

        A comparison of the retrieved SSA above the cloud at the visible wavelengths with the in situ measurements collected
        from the PSAP + TSI nephelometer combination reveals an overall positive bias of ~0.01-0.02 in the satellite retrievals.
        One reason, among several others related to the inherent uncertainties in the satellite-based retrievals, could be the
745   fact that the in situ measurements correspond to the local sampling of smoke particles from instrumentation onboard,
        whereas the satellite retrievals represent columnar, ambient absorption properties of aerosols. The sensitivity analysis
        showed that lowering the assumed AAE in the aerosol model by 0.1-0.2 in the VIS-NIR spectral range could retrieve
        lower SSA (470 nm) by ~0.005-0.01; however, the change is not sufficient to explain the difference between in situ
        and satellite inversions.

750   A similar comparison against the airborne 4STAR inversion of SSA also reveals the tendency of satellite retrievals to
        be biased higher for the September 2016 ORACLES data. The differences were more pronounced at the near-UV
        wavelength of 388 nm than at the 470 nm wavelength. Changing the near-UV aerosol model with reduced spectral
        dependence of absorption brought the observed differences down from ~0.055 to ~0.035—an improvement of 0.02 in
        SSA.

755   One important and promising result we derive in this analysis is the consistency in measuring the intra-seasonal trend
        in the retrieved SSA of smoke transport above clouds over the southeastern Atlantic Ocean. The satellite retrievals,
        ORACLES in situ measurements, and ground-based inversion from AERONET all show stronger absorption strength
        (lower SSA) in August, relatively weaker absorption in September, and even lower absorption (higher SSA) in October.
        Given the inherent uncertainties in all of these measurements, their relative biases, and the imperfections in the
760   methodology, a consistent seasonal trend in SSA captured by different sensors run on distinct inversion methods is
        encouraging, which agrees with the previous studies (e.g., Eck et al., 2013). The level of agreement and consistency
        shown by the airborne-satellite synergy not only increases our confidence in the proposed inversion method but also
        motivates us to expand its application over other regions and even to a global scale, as briefly discussed in the
        following paragraph.

765   The synergy of airborne and satellite sensors and its application demonstrated in this paper opens a possibility of
        synergizing the measurements from NASA's A-train satellite sensors to characterize aerosol absorption above the
        clouds in the UV-VIS spectral domain. For instance, the De-polarization Ratio (DR) method applied to the CALIOP
        532-nm lidar backscatter measurements retrieves ACAOD at 532 nm without involving any assumptions on aerosol
        properties (Hu et al., 2007). The DR method is physically based on the two-way transmission of lidar signal and
770   operates on scenes with opaque liquid water clouds with an assumed value of the cloud lidar ratio. The DR-based
        ACAODs retrieved from CALIOP for a couple of case studies of smoke aerosols above clouds were found to agree
        well with other passive satellite-based retrievals over the Southeastern Atlantic Ocean (Jethva et al., 2016). The DR
        method avoids any assumptions on the intrinsic aerosol properties, whereas other satellite-based retrieval techniques
        of ACAOD based on passive measurements are sensitive to the chosen aerosol model. Therefore, the DR method is
775   expected to deliver a more accurate quantification of aerosol loading above the cloud. Being a part of NASA's A-train

satellite constellation, the CALOP, OMI, and MODIS sensors fly in formation and make measurements within a few minutes of time difference. The proposed synergy algorithm thus should be further tested and adopted for the potential A-train synergy to derive regional and even global, combined retrieval datasets of ACAOD, SSA, and aerosol-corrected COD. The availability of the joint aerosol-cloud product on a global scale will provide unprecedented quantitative information about the optical properties of aerosols and clouds, which play a crucial role in determining the sign and magnitude of the radiative effects of aerosols above clouds. Furthermore, the anticipated satellite synergy retrievals can help constrain the climate models with the much-needed observational estimates of the radiative effects of aerosols in cloudy regions and expand our ability to study aerosol direct and semi-direct effects on clouds and radiation balance.

COMPETING INTERESTS

At least one of the (co-)authors is a member of the editorial board of Atmospheric Measurement Techniques.

ACKNOWLEDGMENTS

The authors acknowledge the efforts of the ORACLES team, both deployment support staff and the science team, for successfully conducting airborne measurements during the 2016 and 2017 campaigns and freely distributing the

790   valuable datasets to the user community on NASA's ESPO web portal https://espo.nasa.gov/oracles. Acknowledgments are also due to the MODIS Adaptive Processing System (MODAPS) and OMI SIPS teams (https://earthdata.nasa.gov/about/sips/sips-modaps) for processing MODIS and OMI L1B datasets used in the present study. The Terra-Aqua/MODIS L1b datasets were acquired from the Level-1 and Atmosphere Archive & Distribution System (LAADS) Distributed Active Archive Center (DAAC), located in the Goddard Space Flight Center in

795   Greenbelt, Maryland (https://ladsweb.nascom.nasa.gov/). The Aura-OMI OMACA product containing L1B data used in this study was obtained from the Aura Validation Data Center at the URL https://avdc.gsfc.nasa.gov/. The AERONET-OMI-MODIS synergy SSA retrieval dataset for the Mongu site used in the study for comparison was obtained from Kayetha et al. (2022). We thank all PI(s) and Co-I(s) and their staff for establishing and maintaining the AERONET sites over central/southern Africa whose datasets are used for the comparison in this study. The present

800   research work was funded by the NASA ROSES-2019 Aura Science Team Call (Solicitation: A.22 NNH19ZDA001N-AURAST) under the grant number NASA Award/Grant Number: 80NSSC20K0946.

805

REFERENCES

Ahn, C., Torres, O., and Jethva, H.: Assessment of OMI near-UV aerosol optical depth over land, J. Geophys. Res. Atmos., 119, doi:10.1002/2013JD020188, 2014.

810

Ahn, C., Torres, O., Jethva, H., Tiruchirapalli, R., & Huang, L.-K. : Evaluation of aerosol properties observed by DSCOVR/EPIC instrument from the Earth-Sun Lagrange 1 Orbit. Journal of Geophysical Research: Atmospheres, 126, e2020JD033651. https://doi.org/10.1029/2020JD033651, 2021.

815   Burton, S. P., Hostetler, C. A., Cook, A. L., Hair, J. W., Seaman, S. T., Scola, S., Harper, D. B., Smith, J. A., Fenn, M. A., Ferrare, R. A., Saide, P. E., Chemyakin, E. V., and Müller, D.: Calibration of a high spectral resolution lidar using a Michelson interferometer, with data examples from ORACLES, Appl. Opt. 57, 6061-6075, 2018.

Chand, D., Anderson, T. L., Wood, R., Charlson, R. J., Hu, Y., Liu, Z., and Vaughan, M.: Quantifying above-cloud
820   aerosol using spaceborne lidar for improved understanding of cloudy-sky direct climate forcing, J. Geophys. Res., 113, D13206, doi:10.1029/2007JD009433, 2008.

Chand, D., Wood, R., Anderson, T. L., Satheesh, S. K., and Charlson, R. J.: Satellite-derived direct radiative effect of aerosols dependent on cloud cover, *Nat. Geosci.*, 2, 181-184, doi:10.1038/ngeo437, 2009.

825

Deirmendjian, D.: Electromagnetic scattering on spherical polydispersions, American Elsevier Publishing Company, Inc., 108 pp., New York, 1969.

Devasthale, A. and Thomas, M. A.: A global survey of aerosol-liquid water cloud overlap based on four years of
830   CALIPSO-CALIOP data, Atmos. Chem. Phys., 11, 1143–1154, https://doi.org/10.5194/acp-11-1143-2011, 2011.

Dubovik, O. and King, M.: A flexible inversion algorithm for retrieval of aerosol optical properties from Sun and sky radiance measurements, J. Geophys. Res.-Atmos., 105, 20673–20696, https://doi.org/10.1029/2000JD900282, 2000.

835   Dubovik, O., Holben, B. N., Eck, T. F., Smirnov, A., Kaufman, Y. J., King, M. D., Tanre, D., and Slutsker, I.: Variability of absorption and optical properties of key aerosol types observed worldwide locations, J. Atmos. Sci., 59, 590–608, 2002.

Dunagan, S. E., Johnson, R., Zavaleta, J., Russell, P. B., Schmid, B., Flynn, C., Redemann, J., Shinozuka, Y.,
840   Livingston, J., Segal-Rosenhaimer, M.: Spectrometer for Sky-Scanning Sun-Tracking Atmospheric Research (4STAR): Instrument Technology, Remote Sens., 5, 3872-3895. https://doi.org/10.3390/rs5083872, 2013.

Graaf, M., Tilstra, L. G., Wang, P., and Stammes, P.: Retrieval of the aerosol direct radiative effect over clouds from spaceborne spectrometry, *J. Geophys. Res.*, 117, D07207, doi:10.1029/2011JD017160, 2012.

845

Eck, T. F., et al.: A seasonal trend of single scattering albedo in southern African biomass-burning particles: Implications for satellite products and estimates of emissions for the world's largest biomass-burning source, *J. Geophys. Res. Atmos.*, 118, 6414-6432, doi:10.1002/jgrd.50500, 2013.

850   Eswaran, K., Satheesh, S. K. and Srinivasan, J.: Dependence of 'critical cloud fraction' on aerosol composition. Atmos. Sci. Lett., 16: 380-385. doi:10.1002/asl2.571, 2015.

Hale, G. and Querry, M.: Optical Constants of Water in the 200-nm to 200-µm Wavelength Region, Appl. Opt., 12, 555–563, 1973.

855   Harshvardhan, H., Ferrare, R., Burton, S., Hair, J., Hostetler, C., Harper, D., Cook, A., Fenn, M., Scarino, A. J., Chemyakin, E., and Müller, D.: Vertical structure of biomass burning aerosol transported over the southeast Atlantic Ocean, Atmos. Chem. Phys., 22, 9859-9876, https://doi.org/10.5194/acp-22-9859-2022, 2022.

860   Holben, B. N., Eck, T. F., Slutsker, I., Tanre, D., Buis, J. P., Setzer A., Vermore, E., Reagan, J. A., Kaufman, Y. J., Nakajima, T., Lavenu, F., Jankowiak, I., and Smirnov, A.: AERONET- a federal instrument network and data archive for aerosol characterization, Remote Sens. Environ., 66, 1–16, 1998.

        Hu, Y., Vaughan, M., Liu, Z., Powell, K., and Rodier, S.: Retrieving Optical Depths and Lidar Ratios for Transparent
865   Layers Above Opaque Water Clouds From CALIPSO Lidar Measurements, *IEEE Geosci. Remote Sens. Lett.*, 4 (4), 523-526, doi: 10.1109/LGRS.2007.901085, 2007.

        IPCC, 2021: Climate Change 2021: The Physical Science Basis. Contribution of Working Group I to the Sixth Assessment Report of the Intergovernmental Panel on Climate Change[Masson-Delmotte, V., P. Zhai, A. Pirani, S.L.
870   Connors, C. Péan, S. Berger, N. Caud, Y. Chen, L. Goldfarb, M.I. Gomis, M. Huang, K. Leitzell, E. Lonnoy, J.B.R. Matthews, T.K. Maycock, T. Waterfield, O. Yelekçi, R. Yu, and B. Zhou (eds.)]. Cambridge University Press, Cambridge, United Kingdom and New York, NY, USA, In press, doi:10.1017/9781009157896.

        Jethva, H. and Torres, O.: Satellite-based evidence of wavelength-dependent aerosol absorption in biomass burning smoke inferred from Ozone Monitoring Instrument, Atmos. Chem. Phys., 11, 10541-10551,
875   https://doi.org/10.5194/acp-11-10541-2011, 2011.

        Jethva, H., Torres, O., Remer, L. A., Bhartia, P. K.: A Color Ratio Method for Simultaneous Retrieval of Aerosol and Cloud Optical Thickness of Above-Cloud Absorbing Aerosols From Passive Sensors: Application to MODIS Measurements, *IEEE Trans. Geosci. Rem. Sens.*, 51 (7), 3862-3870, doi: 10.1109/TGRS.2012.2230008, 2013.

        Jethva, H., Torres, O., and Ahn, C.: Global assessment of OMI aerosol single-scattering albedo using ground-based
880   AERONET inversion, J. Geophys. Res. Atmos., 119, 9020-9040, doi:10.1002/2014JD021672, 2014.

        Jethva, H., Torres, O., Remer, L., Redemann, J., Livingston, J., Dunagan, S., Shinozuka, Y., Kacenelenbogen, M., Rosenheimer, M. S., and Spurr, R.: Validating MODIS above-cloud aerosol optical depth retrieved from "color ratio" algorithm using direct measurements made by NASA's airborne AATS and 4STAR sensors, Atmos. Meas. Tech., 9, 5053–5062, https://doi.org/10.5194/amt-9-5053-2016, 2016.

885   Jethva, H., Torres, O., and Ahn, C.: A 12-year long global record of optical depth of absorbing aerosols above the clouds derived from the OMI/OMACA algorithm, Atmos. Meas. Tech., 11, 5837-5864, https://doi.org/10.5194/amt-11-5837-2018, 2018.

        Kacenelenbogen, M. S., Vaughan, M. A., Redemann, J., Young, S. A., Liu, Z., Hu, Y., Omar, A. H., LeBlanc, S., Shinozuka, Y., Livingston, J., Zhang, Q., and Powell, K. A.: Estimations of global shortwave direct aerosol radiative
890   effects above opaque water clouds using a combination of A-Train satellite sensors, Atmos. Chem. Phys., 19, 4933–4962, https://doi.org/10.5194/acp-19-4933-2019, 2019.

        Kaufman, Y. J., Koren, I., Remer, L. A., Tanré, D., Ginoux, P., and Fan, S.: Dust transport and deposition observed from the Terra-Moderate Resolution Imaging Spectroradiometer (MODIS) spacecraft over the Atlantic Ocean, *J. Geophys. Res.*, 110, D10S12, doi:10.1029/2003JD004436, 2005.

895   Kayetha, V., Torres, O., and Jethva, H.: Retrieval of UV–visible aerosol absorption using AERONET and OMI–MODIS synergy: spatial and temporal variability across major aerosol environments, Atmos. Meas. Tech., 15, 845–877, https://doi.org/10.5194/amt-15-845-2022, 2022.

Keil, A., and Haywood, J. M.: Solar radiative forcing by biomass burning aerosol particles during SAFARI 2000: A case study based on measured aerosol and cloud properties, *J. Geophys. Res.*, 108, 8467, doi:10.1029/2002JD002315, D13, 2003.

Kirchstetter, T. W., Novakov, T., and Hobbs, P. V.: Evidence that the spectral dependence of light absorption by aerosols is affected by organic carbon, *J. Geophys. Res.*, 109, D21208, doi:10.1029/2004JD004999, 2004.

Kurosu, T. P. and Celarier, E. A.: OMI/Aura Global Ground Pixel Corners 1-Orbit L2 Swath 13x24km V003, Greenbelt, MD, USA, Goddard Earth Sciences Data and Information Services Center (GES DISC), Accessed: Jan 10, 2019, 10.5067/Aura/OMI/DATA2020, 2010.

LeBlanc, S. E., Redemann, J., Flynn, C., Pistone, K., Kacenelenbogen, M., Segal-Rosenheimer, M., Shinozuka, Y., Dunagan, S., Dahlgren, R. P., Meyer, K., Podolske, J., Howell, S. G., Freitag, S., Small-Griswold, J., Holben, B., Diamond, M., Wood, R., Formenti, P., Piketh, S., Maggs-Kölling, G., Gerber, M., and Namwoonde, A.: Above-cloud aerosol optical depth from airborne observations in the southeast Atlantic, Atmos. Chem. Phys., 20, 1565–1590, https://doi.org/10.5194/acp-20-1565-2020, 2020.

Levelt, P. F. et al.: The ozone monitoring instrument, *IEEE Trans. Geosci. Remote Sens.*, 44 (5), 1093-1101, doi: 10.1109/TGRS.2006.872333, 2006.

Meyer, K., Platnick, S., and Zhang, Z.: Simultaneously inferring above-cloud absorbing aerosol optical thickness and underlying liquid phase cloud optical and microphysical properties using MODIS, *J. Geophys. Res. Atmos.*, 120, 5524-5547. doi: 10.1002/2015JD023128, 2015.

Platnick, S. et al.: The MODIS Cloud Optical and Microphysical Products: Collection 6 Updates and Examples From Terra and Aqua, *IEEE Trans. Geosci. Remote Sens.*, 55 (1), 502-525, doi: 10.1109/TGRS.2016.2610522, 2017.

Peers, F., Waquet, F., Cornet, C., Dubuisson, P., Ducos, F., Goloub, P., Szczap, F., Tanré, D., and Thieuleux, F.: Absorption of aerosols above clouds from POLDER/PARASOL measurements and estimation of their direct radiative effect, Atmos. Chem. Phys., 15, 4179–4196, https://doi.org/10.5194/acp-15-4179-2015, 2015.

Pistone, K., Redemann, J., Doherty, S., Zuidema, P., Burton, S., Cairns, B., Cochrane, S., Ferrare, R., Flynn, C., Freitag, S., Howell, S. G., Kacenelenbogen, M., LeBlanc, S., Liu, X., Schmidt, K. S., Sedlacek III, A. J., Segal-Rozenhaimer, M., Shinozuka, Y., Stamnes, S., van Diedenhoven, B., Van Harten, G., and Xu, F.: Intercomparison of biomass burning aerosol optical properties from in situ and remote-sensing instruments in ORACLES-2016, Atmos. Chem. Phys., 19, 9181–9208, https://doi.org/10.5194/acp-19-9181-2019, 2019.

Prospero, J. M., Ginoux, P., Torres, O., Nicholson, S. E., and Gill, T. E.: Environmental Characterization Of Global Sources Of Atmospheric Soil Dust Identified With The Nimbus 7 Total Ozone Mapping Spectrometer (Toms) Absorbing Aerosol Product, *Rev. Geophys.*, 40 (1), 1002, doi:10.1029/2000RG000095, 2002.

Redemann, J., Wood, R., Zuidema, P., Doherty, S. J., Luna, B., LeBlanc, S. E., Diamond, M. S., Shinozuka, Y., Chang, I. Y., Ueyama, R., Pfister, L., Ryoo, J.-M., Dobracki, A. N., da Silva, A. M., Longo, K. M., Kacenelenbogen, M. S., Flynn, C. J., Pistone, K., Knox, N. M., Piketh, S. J., Haywood, J. M., Formenti, P., Mallet, M., Stier, P., Ackerman, A. S., Bauer, S. E., Fridlind, A. M., Carmichael, G. R., Saide, P. E., Ferrada, G. A., Howell, S. G., Freitag, S., Cairns, B., Holben, B. N., Knobelspiesse, K. D., Tanelli, S., L'Ecuyer, T. S., Dzambo, A. M., Sy, O. O., McFarquhar, G. M., Poellot, M. R., Gupta, S., O'Brien, J. R., Nenes, A., Kacarab, M., Wong, J. P. S., Small-Griswold, J. D., Thornhill, K. L., Noone, D., Podolske, J. R., Schmidt, K. S., Pilewskie, P., Chen, H., Cochrane, S. P., Sedlacek, A. J., Lang, T. J., Stith, E., Segal-Rozenhaimer, M., Ferrare, R. A., Burton, S. P., Hostetler, C. A., Diner, D. J., Seidel, F. C., Platnick, S. E., Myers, J. S., Meyer, K. G., Spangenberg, D. A., Maring, H., and Gao, L.: An overview of the ORACLES (ObseRvations of Aerosols above CLouds and their intEractionS) project: aerosol–cloud–radiation interactions in the southeast Atlantic basin, Atmos. Chem. Phys., 21, 1507–1563, https://doi.org/10.5194/acp-21-1507-2021, 2021.

940   Russell, P. B., Bergstrom, R. W., Shinozuka, Y., Clarke, A. D., DeCarlo, P. F., Jimenez, J. L., Livingston, J. M., Redemann, J., Dubovik, O., and Strawa, A.: Absorption Angstrom Exponent in AERONET and related data as an indicator of aerosol composition, *Atmos. Chem. Phys.*, 10, 1155-1169, https://doi.org/10.5194/acp-10-1155-2010, 2010.

        Schulz, M., Textor, C., Kinne, S., Balkanski, Y., Bauer, S., Berntsen, T., Berglen, T., Boucher, O., Dentener, F.,
945   Guibert, S., Isaksen, I. S. A., Iversen, T., Koch, D., Kirkevåg, A., Liu, X., Montanaro, V., Myhre, G., Penner, J. E., Pitari, G., Reddy, S., Seland, Ø., Stier, P., and Takemura, T.: Radiative forcing by aerosols as derived from the AeroCom present-day and pre-industrial simulations, *Atmos. Chem. Phys.*, 6, 5225-5246, doi:10.5194/acp-6-5225-2006, 2006.

950   Segal-Rosenheimer, M., Russell, P. B., Schmid, B., Redemann, J., Livingston, J. M., Flynn, C. J., Johnson, R. R., Dunagan, S. E., Shinozuka, Y., Herman, J., Cede, A., Abuhassan, N., Comstock, J. M., Hubbe, J. M., Zelenyuk, A., Wilson, J.: Tracking elevated pollution layers with a newly developed hyperspectral Sun/Sky spectrometer (4STAR): Results from the TCAP 2012 and 2013 campaigns, J. Geophys. Res. Atmos., 119, 2611– 2628, doi:10.1002/2013JD020884, 2014.

955

        Shinozuka, Y., Johnson, R. R., Flynn, C. J., Russell, P. B., Schmid, B., Redemann, J., Dunagan, S. E., Kluzek, C. D., Hubbe, J. M., Segal-Rosenheimer, M., Livingston, J. M., Eck, T. F., Wagener, R., Gregory, L., Chand, D., Berg, L. K., Rogers, R. R., Ferrare, R. A., Hair, J. W., Hostetler, C. A., Burton, S. P.: Hyperspectral aerosol optical depths from TCAP flights, J. Geophys. Res. Atmos., 118, 12,180– 12,194, doi:10.1002/2013JD020596, 2013.

960

        Spurr, R. J. D.: A linearized pseudo-spherical vector discrete ordinate radiative transfer code for forward model and retrieval studies in multilayer multiple scattering media, J. Quant. Spectrosc. Radiat. Transf., 102 (2), 316-342, http://dx.doi.org/10.1016/j.jqsrt.2006.05.005, 2006.

        Torres, O., Bhartia, P. K., Sinyuk, A., Welton, E. J., and Holben, B.: Total Ozone Mapping Spectrometer
965   measurements of aerosol absorption from space: Comparison to SAFARI 2000 ground-based observations, *J. Geophys. Res.*, 110, D10S18, doi:10.1029/2004JD004611, 2005.

        Torres, O., Tanskanen, A., Veihelmann, B., Ahn, C., Braak, R., Bhartia, P. K., Veefkind, P., and Levelt, P.: Aerosols and surface UV products from Ozone Monitoring Instrument observations: An overview, *J. Geophys. Res.*, 112, D24S47, doi:10.1029/2007JD008809, 2007.

970   Torres, O., Jethva, H., and Bhartia, P. K.: Retrieval of aerosol optical depth above clouds from OMI observations: Sensitivity analysis and case studies, *J. Atmos. Sci.*, 69 (3), 1037-1053, doi: http://dx.doi.org/10.1175/JAS-D-11-0130, 2012.

        Torres, O., Ahn, C., and Chen, Z.: Improvements to the OMI near-UV aerosol algorithm using A-train CALIOP and
975   AIRS observations, Atmos. Meas. Tech., 6, 3257-3270, https://doi.org/10.5194/amt-6-3257-2013, 2013.

        Torres, O., Jethva, H., Ahn, C., Jaross, G., and Loyola, D. G.: TROPOMI aerosol products: evaluation and observations of synoptic-scale carbonaceous aerosol plumes during 2018–2020, Atmos. Meas. Tech., 13, 6789–6806, https://doi.org/10.5194/amt-13-6789-2020, 2020.
980

        Virkkula, A.: Correction of the Calibration of the 3-wavelength Particle Soot Absorption Photometer (3 PSAP), Aerosol Sci. Tech., 44, 706–712, https://doi.org/10.1080/02786826.2010.482110, 2010.

985 Waquet, F., Riedi, J., Labonnote, L. C., Goloub, P., Cairns, B., Deuzé, J., and Tanré, D.: Aerosol Remote Sensing over Clouds Using A-Train Observations, J. Atmos. Sci., 66, 2468-2480, https://doi.org/10.1175/2009JAS3026.1, 2009.

Wilcox, E. M., Harshvardhan, and Platnick, S.: Estimate of the impact of absorbing aerosol over cloud on the MODIS retrievals of cloud optical thickness and effective radius using two independent retrievals of liquid water path, *J. Geophys. Res.*, 114, D05210, doi:10.1029/2008JD010589, 2009.

990 Wilcox, E. M.: Direct and semi-direct radiative forcing of smoke aerosols over clouds, *Atmos. Chem. Phys*., 12, 139-149, https://doi.org/10.5194/acp-12-139-2012, 2012.

Zhang, Z., Meyer, K., Yu, H., Platnick, S., Colarco, P., Liu, Z., and Oreopoulos, L.: Shortwave direct radiative effects of above-cloud aerosols over global oceans derived from 8 years of CALIOP and MODIS observations, Atmos. Chem. Phys., 16, 2877–2900, https://doi.org/10.5194/acp-16-2877-2016, 2016.

995 Zuidema, P., Redemann, J., Haywood, J., Wood, R., Piketh, S., Hipondoka, M., and Formenti, P.: Smoke and Clouds above the Southeast Atlantic: Upcoming Field Campaigns Probe Absorbing Aerosol's Impact on Climate. Bull. Amer. Meteor. Soc., 97, 1131–1135, https://doi.org/10.1175/BAMS-D-15-00082.1, 2016.

LIST OF TABLES

Table 1. Airborne-satellite sensors and their respective datasets used in the present study.

1000 **Table 2.** Optical-microphysical properties of the carbonaceous aerosol model and radiative transfer configurations adopted in the synergy inversion algorithm. The model numbers are ordered from most absorbing to most scattering aerosols. AAE represents the Absorption Ångström Exponent for the UV (354-388 nm) and VIS-NIR (470-860 nm) wavelength domains.

Table 3. Uncertainties in the retrieved SSA at the 388 nm wavelength of OMI due to errors in the algorithmic input
1005 parameters. Uncertainties are estimated by comparing the SSA retrievals from September 2016 OMI-HSRL2 collocated measurements derived assuming the perturbed input parameters against those retrieved from original, unperturbed input parameters. m and s represent the average and standard deviation of errors.

Table 4. Same as in Table 4 but for the retrieved SSA at the 470 nm wavelength of MODIS for the collocated dataset of MODIS-HSRL2 measurements for Aug-Sep 2016.

1010

Table 1 Airborne-satellite sensors and their respective datasets used in the present study.

Platform/ Instrument	Operation Period	Measurement Characteristics
ER2/HSRL-2	ORACLES Phase I (Aug-Sep 2016)[1]	Detailed vertical profile of aerosol backscatter and extinction Above-cloud column aerosol optical depth at 355 nm and 532 nm Dataset version: R9 (2016), R1 (2017), R1 (2018)
P3-Orion/4STAR P3-Orion/HSRL-2	ORACLES Phase 1 (Aug-Sep 2016)[1] Phase 2 (Aug-Sep 2017)[2] Phase 3 (Sep-Oct 2018)[3]	Direct Sun measurements of spectral aerosol optical depth 4STAR dataset version: R4 (2016), R1 (2017), R1 (2018) 4STAR sky scan inversion of spectral SSA R1 (2016), R0 (2017)
P3-Orion/PSAP+TSI Nephelometer	Phase 1 (Aug-Sep 2016)[1] Phase 2 (Aug-Sep 2017)[2] Phase 3 (Sep-Oct 2018)[3]	HiGEAR onboard in situ measurements of aerosol SSA Version: R2 for all three years
Aura/OMI	Collocated in space and time with ORACLES observations	L1B top-of-atmosphere reflectance at 354 nm and 388 nm at nadir pixel resolution of 13x24 km^2 OMACA Level-2 product for identification of above-cloud aerosols scene
Terra-Aqua /MODIS	Collocated in space and time with ORACLES campaigns	L1B top-of-atmosphere reflectance at 470 nm and 860 nm (MOD/MYD021KM) Geolocation and geometry (MOD/MYD03) L2 cloud product (MOD/MYD06_L2) 1-km measurements averaged to 5-km nominal grid

[1]**ORACLES-1 Aug-Sep 2016**
4STAR on P3-Orion flights (Total 12): Aug 27, 30, 31; Sep 02, 08, 10, 14, 18, 20, 24, 25, 27
HSRL-2 on ER-2 flights (total 7): Aug 26, Sep 12, 16, 18, 20, 22, 24

[2]**ORACLES-2 Aug-Sep 2017**
HSRL-2/4STAR on P3-Orion flights (Total 15): Aug 09, 12, 13, 15, 17, 18, 19, 21, 24, 26, 28, 30, 31; Sep 02, 03

[3]**ORACLES-3 Sep-Oct 2018**
HSRL-2/4STAR on P3-Orion flights (Total 15): Sep 24, 27, 30; Oct 02, 03, 05, 07, 10, 12, 15, 17, 19, 21, 23, 25

1015   **Table 2** Optical-microphysical properties of the carbonaceous aerosol model and radiative transfer configurations adopted in the synergy inversion algorithm. The model numbers are ordered from most absorbing to most scattering aerosols. AAE represents the Absorption Ångström Exponent for the UV (354-388 nm) and VIS-NIR (470-860 nm) wavelength domains.

Model Number	Imaginary Index				Single-scattering Albedo				AAE	AAE
	354 nm	388 nm	470 nm	860 nm	354 nm	388 nm	470 nm	860 nm	354-388 nm	470-860 nm
1	0.054	0.045	0.050	0.042	0.7729	0.7965	0.7635	0.6769	2.45075	1.2799
2	0.048	0.040	0.045	0.037	0.7914	0.8135	0.7805	0.7003	2.47316	1.2809
3	0.042	0.035	0.040	0.032	0.8109	0.8312	0.7983	0.7257	2.49355	1.2877
4	0.036	0.030	0.035	0.026	0.8316	0.8499	0.8171	0.7597	2.51118	1.3447
5	0.030	0.025	0.030	0.022	0.8535	0.8696	0.8369	0.7848	2.52527	1.3380
6	0.024	0.020	0.025	0.018	0.8769	0.8905	0.8578	0.8125	2.53511	1.3380
7	0.018	0.015	0.020	0.015	0.9020	0.9129	0.8802	0.8353	2.54113	1.2692
8	0.012	0.010	0.015	0.012	0.9293	0.9373	0.9043	0.8603	2.55022	1.1695
9	0.006	0.005	0.010	0.008	0.9602	0.9648	0.9308	0.8980	2.59644	1.1536
10	0.000	0.000	0.005	0.004	1.0000	1.0000	0.9612	0.9429	N/A	1.1566

Real refractive index = 1.5

Mean Radius (fine mode) = 0.0898 µm   Mean Radius (coarse mode) = 0.9444 µm
Standard Deviation (fine mode) = 1.4896 µm   Standard Deviation (coarse mode) = 1.9326 µm

Nodes of above-cloud aerosol LUTs
ACAOD (500 nm) = [0.0, 0.1, 0.25, 0.50, 0.75 1.00, 1.50, 2.00, 3.0, 5.0]
COD (wavelength-independent) = [0, 2, 5, 10, 20, 30, 40, 50]
Extinction Ångström Exponent (354-500) = 1.48
Extinction Ångström Exponent (470-860) = 1.80
Solar Zenith Angle (7) = [0°, 10°, 20°, 30°, 40°, 50°, 60°]
Viewing Zenith Angle (14) = [0°, 12°, 18°, 26°, 32°, 36°, 40°, 46°, 50°, 54°, 56°, 60°, 66°, 72°]
Relative Azimuth Angle (14) = [0°, 30°, 60°, 90°, 120°, 150°, 160°,165°,170°,175°,180°]
Aerosol Layer Height (3) = [3.0, 4.0, 5.0] in km
Surface Pressure Level = 1013.25 hPa
Surface Albedo (354-388) = 0.05
Surface Albedo (470-860) = 0.03

1020

Table 3 Uncertainties in the retrieved SSA at the 388 nm wavelength of OMI due to errors in the algorithmic input parameters. Uncertainties are estimated by comparing the SSA retrievals from September 2016 OMI-HSRL2 collocated measurements derived assuming the perturbed input parameters against those retrieved from original, unperturbed input parameters. μ and σ represent the average and standard deviation of errors.

	Uncertainties in SSA (388 nm) due to change in AOD (388 nm) ΔAOD							
	-40%	**-20%**	**-10%**	**-5%**	**+5%**	**+10%**	**+20%**	**+40%**
ΔSSA μ±σ	-0.052± 0.011	-0.017± 0.006	-0.008± 0.003	-0.004± 0.001	0.004± 0.001	0.007± 0.003	0.015± 0.005	0.029± 0.009
	Uncertainties in SSA (388 nm) due to change in ALH							
	ΔALH=-1 km				**ΔALH=+1 km**			
ΔSSA μ±σ	-0.008±0.003				0.005±0.002			
	Uncertainties in SSA (388 nm) due to change in AAE *ΔAAE corresponds to ±10% change in imaginary index at 354 nm							
	*ΔAAE=-0.73				***ΔAAE=+0.67**			
ΔSSA μ±σ	-0.029±0.005				0.020±0.004			
	Uncertainties in SSA (388 nm) due to change in Fine Mode Radius [µm]							
	-20%				**+20%**			
ΔSSA μ±σ	0.002±0.001				0.008±0.009			
	Uncertainties in SSA (388 nm) due to change in Real Part of Refractive Index							
	-5%				**+5%**			
ΔSSA μ±σ	+0.011±0.002				-0.015±0.016			
	Uncertainties in SSA (388 nm) due to not accounting for NO2							
	0.25 DU				**0.50 DU**			
ΔSSA μ±σ	+0.001±0.001							

1025

Table 4 Same as in Table 3 but for the retrieved SSA at the 470 nm wavelength of MODIS for the collocated dataset of MODIS-HSRL2 measurements for Aug-Sep 2016.

	Uncertainties in SSA (470 nm) due to change in AOD (470 nm) ΔAOD							
	-40%	**-20%**	**-10%**	**-5%**	**+5%**	**+10%**	**+20%**	**+40%**
ΔSSA μ±σ	-0.031± 0.020	-0.012± 0.008	-0.006± 0.004	-0.003± 0.002	0.003± 0.002	0.005± 0.003	0.010± 0.006	0.018± 0.010
	Uncertainties in SSA (470 nm) due to change in ALH							
	ΔALH=-1 km				**ΔALH=+1 km**			
ΔSSA μ±σ	-0.001±0.001				0.002±0.002			
	Uncertainties in SSA (470 nm) due to change in AAE *ΔAAE corresponds to ±10% change in imaginary index at 860 nm							
	*ΔAAE=-0.12				***ΔAAE=+0.12**			
ΔSSA μ±σ	-0.005±0.001				0.005±0.001			
	Uncertainties in SSA (470 nm) due to change in Fine Mode Radius [μm]							
	-20%				**+20%**			
ΔSSA μ±σ	0.022±0.0035				0.004±0.006			
	Uncertainties in SSA (470 nm) due to change in Real Part of Refractive Index							
	-5%				**+5%**			
ΔSSA μ±σ	0.03±0.004				-0.01±0.006			
	Uncertainties in SSA (388 nm) due to not accounting for NO2							
	0.25 DU				**0.50 DU**			
ΔSSA μ±σ	-0.006±0.002				-0.011±0.004			

Figure 8. Spectral SSA retrieved from satellite-airborne synergy for the ORACLES-1 (top), -2 (middle), and -3 (bottom) campaigns. Retrievals are shown as a standard box-whisker plot format, where the mean and median are presented as filled circles and horizontal lines; shaded boxes represent data points contained between 25 and 75 percentiles; and thin vertical lines as 1.5 times interquartile range (75 minus 25 percentile). In-situ airborne measurements of SSA from PSAP and Nephelometer sensors for the respective ORACLES periods are shown as red circles, whereas spectral SSA inversions from AERONET over inland stations are depicted using different symbols in black. Retrievals of spectral SSA from a research technique combining ground-based AERONET AOD measurements and satellite observations from OMI and MODIS over the inland site *Mongu* in *Zambia* are shown as asterisks.

Figure 9 Comparison of spacetime collocated above-cloud aerosol SSA retrieved from OMI (388 nm) against those derived from 4STAR sunphotometer sky scan observations for the ORACLES-1 September 2016 campaign. The OMI SSA retrievals using the original aerosol model (a, left) with 20% relative spectral dependence in the imaginary part of the refractive index (AAE ~2.45-2.60) and modified aerosol model (b, right) with 10% spectral dependence in the imaginary index (AAE ~1.72-187) are evaluated against those of 4STAR inversions. The OMI-4STAR matchups are color-coded according to the date of observations shown in legends. The arbitrary size of the circles represents the magnitude of coincident AOD (500 nm). The statistical measures of the comparison are printed in the lower left of each plot.

Figure 10. Comparison of spacetime collocated above-cloud aerosol SSA retrieved from MODIS at 470 nm (left column) and 660 nm (right column) against those derived from 4STAR sunphotometer sky scan observations for the ORACLES-1 September 2016 (a, b) and ORACLES-2 August 2017 (c, d) campaigns. The MODIS-4STAR matchups are color-coded according to the date of observations shown in legends. The arbitrary size of the circles represents the magnitude of coincident AOD (500 nm). The statistical measures of the comparison are printed in the lower left of each plot.

Figure 11. A Comparison of the aerosol-corrected (y-axis) and non-corrected (apparent) cloud optical depths retrieved from the present synergy algorithm at 388 nm (red) and 860 nm (blue). The combined retrieval dataset derived from HSRL-2 and 4STAR synergy with OMI and MODIS for all three years of ORACLES campaigns (2016, 2017, and 2018) is used. The solid lines represent linear regression fits calculated from OMI (red) and MODIS (blue) retrievals, respectively. A similar comparison graph shown in the inset relates the aerosol-corrected cloud optical depth retrieved from the present work (y-axis) with that obtained from the OMI-OMACA standard product.

Figure 12. Uncertainty estimates of derived SSA at 388 nm (left) and 470 nm (right) calculated by contrasting the original OMI-MODIS-HSRL-2 collocated retrievals for the 2016 campaign against those retrieved using perturbed ACAOD (red), assumed aerosol layer height (ALH, blue), and relative spectral dependence in absorption or AAE (green). The absolute change in SSA was calculated as perturbed minus original retrievals.
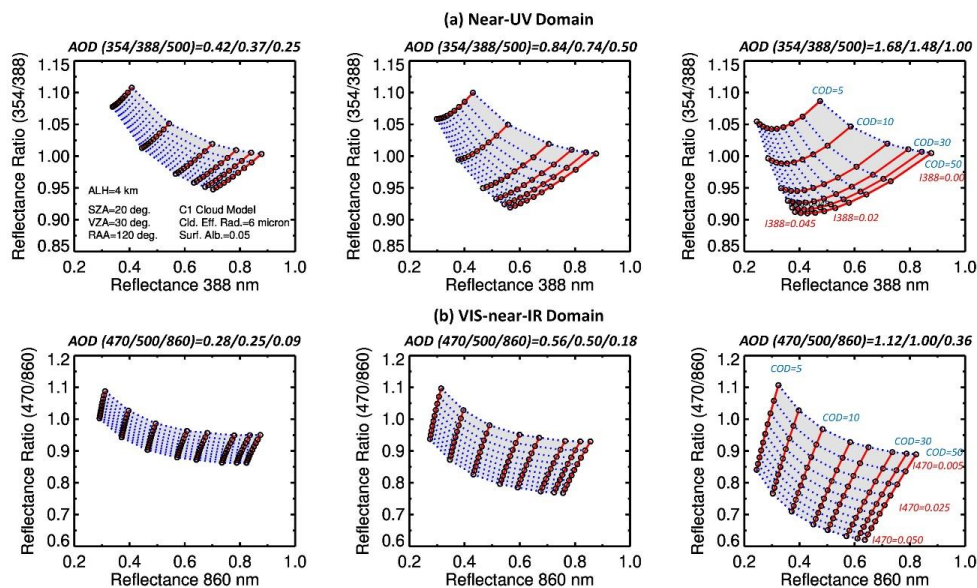
Figure 1 Radiative transfer simulations of TOA reflectance in the a) near-UV (354-388 nm) and b) visible-near-infrared (470-860 nm) wavelength domains of an assumed atmosphere constituted by above-cloud carbonaceous aerosols with varying magnitudes of the imaginary part of the refractive index and COD. The simulation is carried out for the solar zenith, viewing zenith, and relative azimuth angles of 20°, 30°, 120°, respectively, and assumed an aerosol layer with a quasi-Gaussian profile with peak concentration at 4 km above sea level placed above a half-kilometer thick cloud deck located between 850 hPa and 900 hPa. Three scenarios of aerosol loading are presented, i.e., ACAOD of 0.25, 0.5, and 1.0 at 500 nm; ACAODs at other wavelengths were adjusted following the assumed spectral dependence of aerosol extinction. Solid (dotted) curves connecting simulations for the different values of the imaginary index (COD) represent sensitivity to aerosol absorption (cloud brightness).
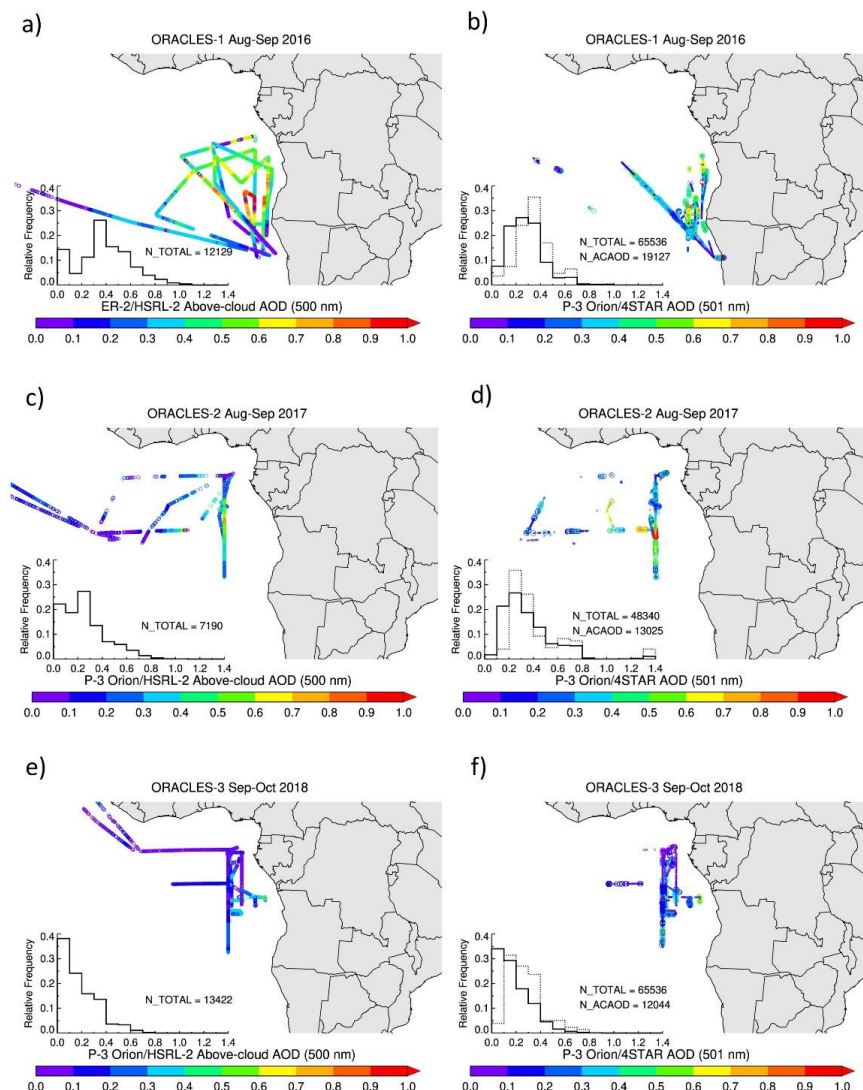
1110

Figure 2. Flight tracks of airborne HSRL-2 (a, c, e) and 4STAR (b, d, f) sensors onboard ER-2 and P3-Orion aircrafts color coded with the measured above-cloud AOD (500 nm) acquired during ORACLES-1 (top row), -2 (middle row), and -3 (bottom row) campaigns in August-September 2016, August-September 2017, and September-October 2018. The histograms of the measured AOD are shown as insets in each plot. The dotted histograms of 4STAR (b, d, f)

1115 represent the measured AOD when the P3 aircraft flew just above the cloud top and beneath the aerosol layer above it, whereas the solid, black-colored histograms show all measurements.
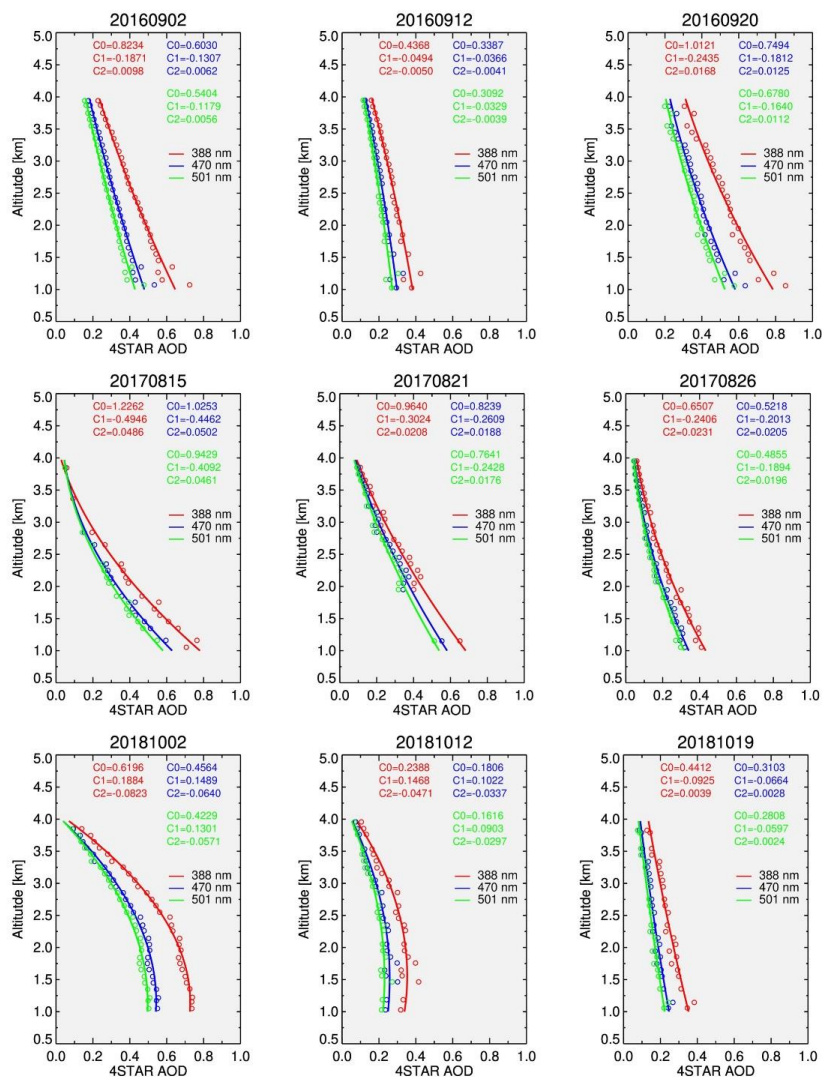
Figure 3. Altitude-averaged vertical profiles (colored circles) of spectral AOD of columnar atmosphere above the aircraft at 388 nm (red), 470 nm (blue), and 501 nm (green) wavelengths measured by 4STAR sunphotometer onboard P3-Orion flights operated on select dates during the ORACLES-1 (top row), -2 (middle row), and -3 (bottom row) campaigns. AOD measurements were aggregated for each altitude grid of size 0.1 km between 1.0 km and 4.0 km using the data for the entire flight to derive an averaged vertical profile and associated altitude versus AOD quadratic polynomial. Coefficients of fitted quadratic relation for the three wavelengths are printed within each plot.
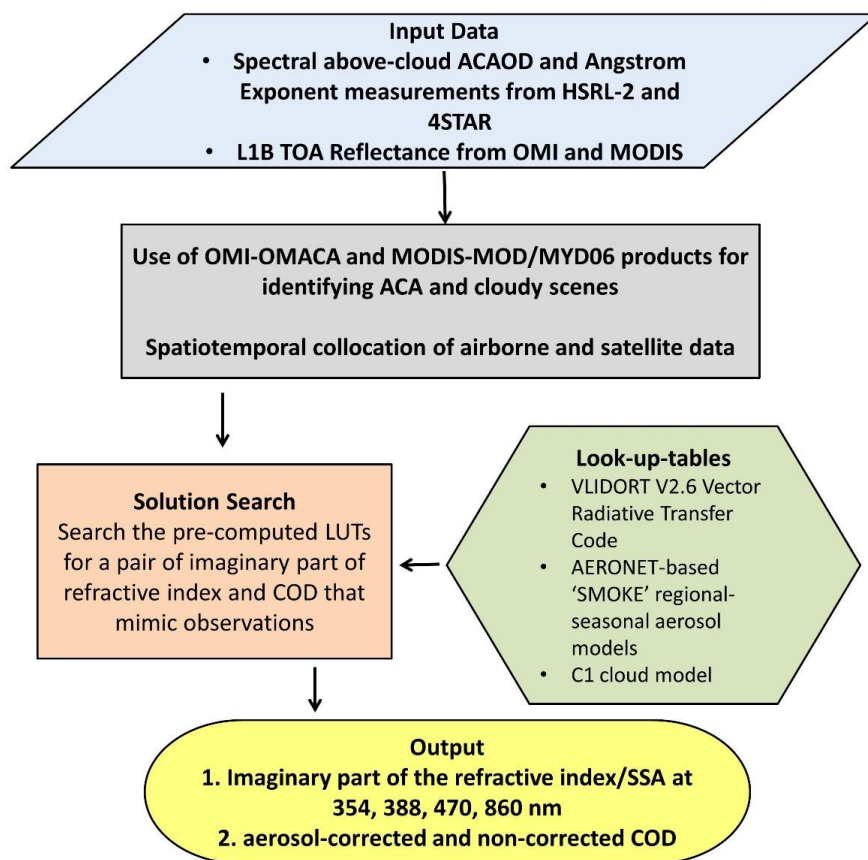
Figure 4 A simplified flowchart of the proposed airborne-satellite synergy algorithm for the retrieval of above-cloud aerosol SSA.

1125
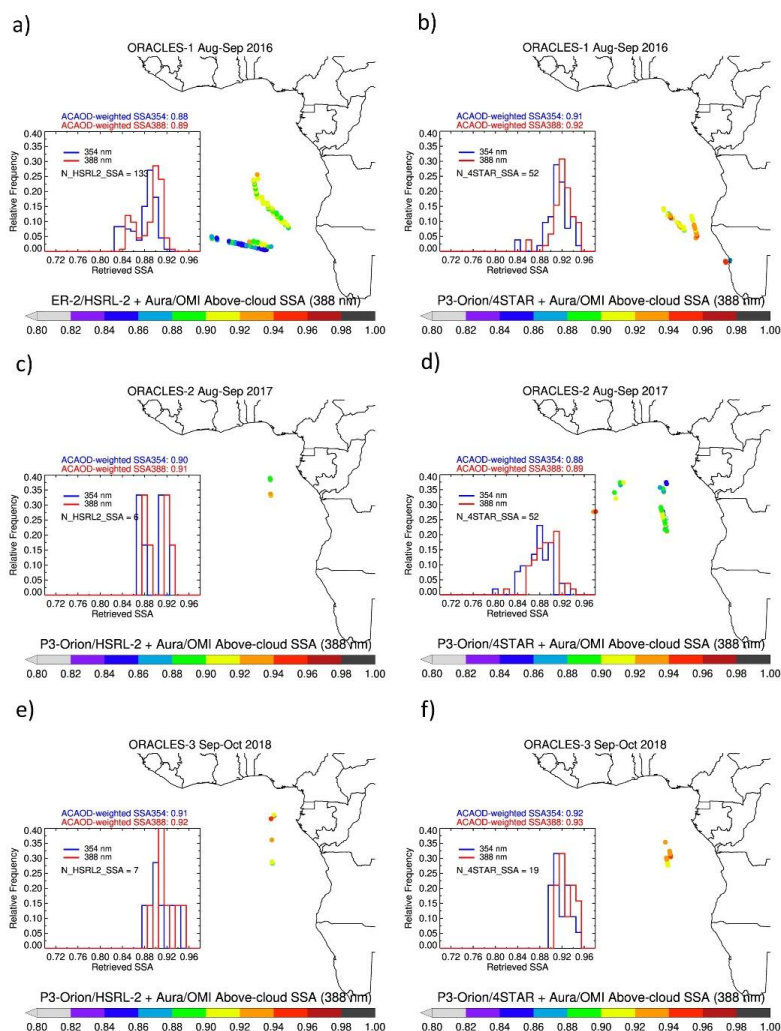
Figure 5. Spatial distribution of above-cloud aerosol SSA at 388 nm retrieved from the collocated measurements of OMI radiances and airborne HSRL-2/4STAR ACAOD (>0.2 at 500 nm) for ORACLES-1 (top row-a, b), -2 (middle row-c, d), and -3 (bottom row-e, f) deployments. Histograms of the retrieved spectral SSA are also shown.
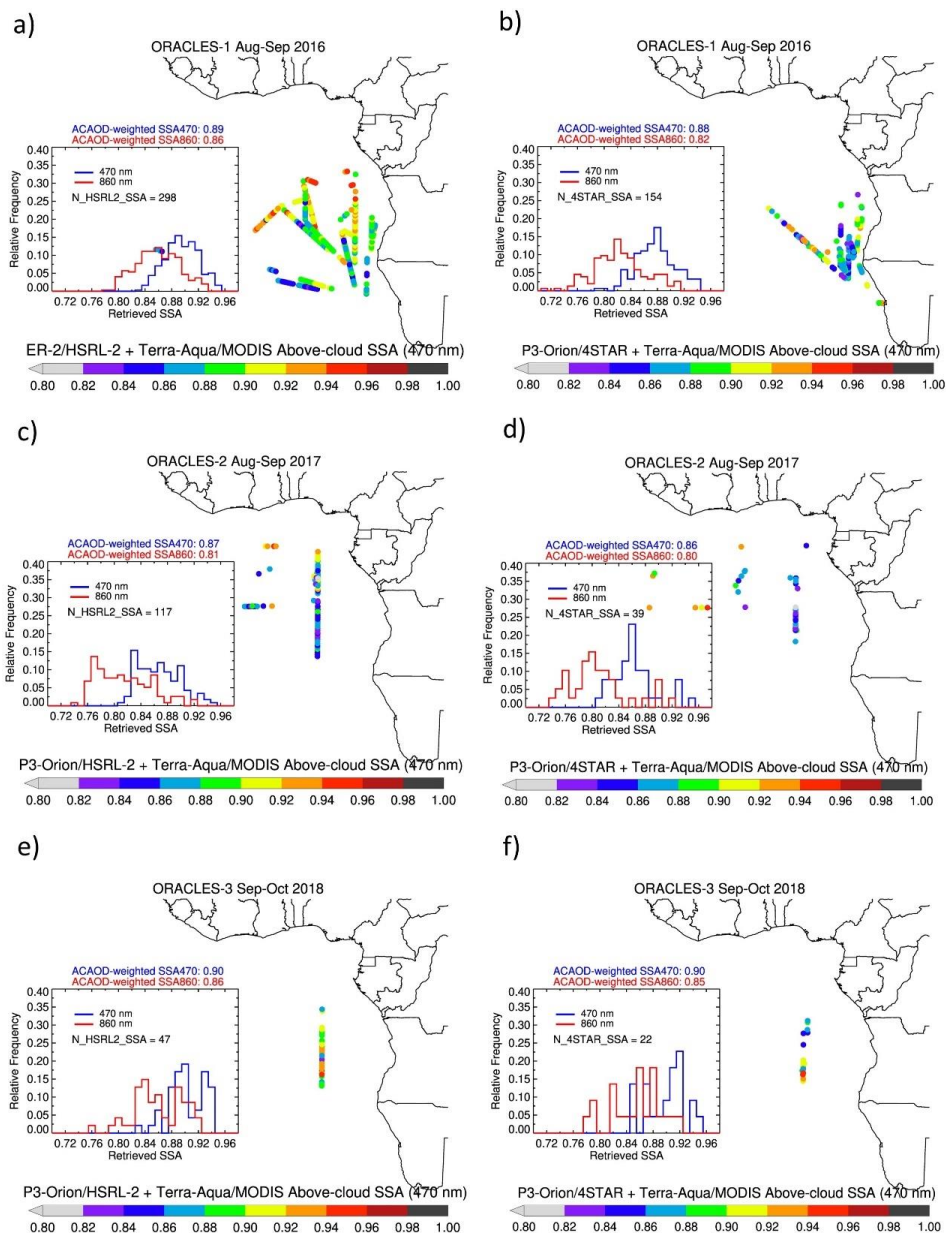
Figure 6 Same as in Figure 5 but for the above-cloud aerosol SSA at 470 nm retrieved from the collocated measurements of MODIS and HSRL-2/4STAR sensors.
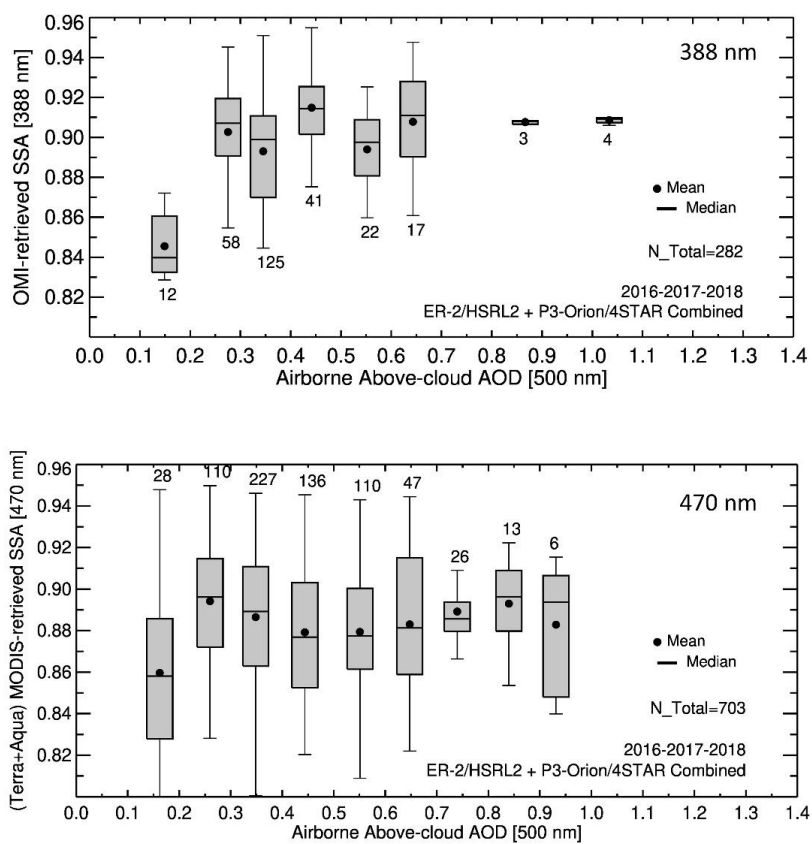
Figure 7 Satellite-retrieved above-cloud aerosol SSA at 388 nm (top) and 470 nm (bottom) as a function of coincident airborne ACAODs used as input to the inversion algorithm. The data are represented as a box-whisker plot for each 0.1 bin size in ACAOD. The number of data points obtained for each bin of ACAOD is shown at the top of the whisker. The satellite-airborne collocated datasets obtained from both HSRL-2 and 4STAR for all three years of the ORACLES deployments are combined and included.
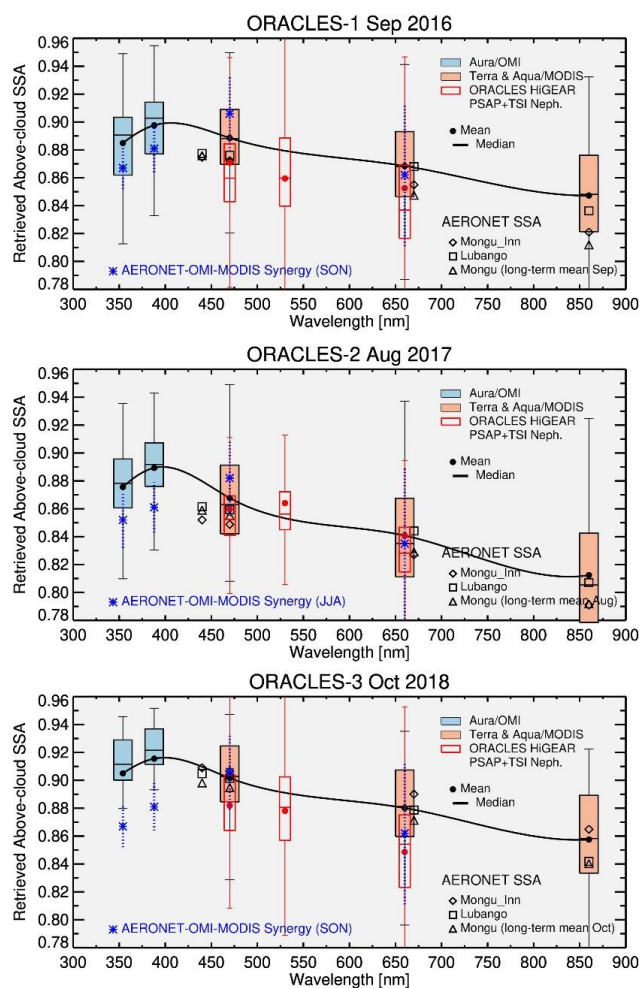
1145

Figure 8. Spectral SSA above clouds retrieved from the combined OMI-MODIS synergy with both HSRL-2 and 4STAR for the ORACLES-1 (top), -2 (middle), and -3 (bottom) deployments. Retrievals are shown as a box-whisker plot format, where the mean and median are presented as filled circles and horizontal lines; shaded boxes represent data points contained between 25 and 75 percentiles; and thin vertical lines as 1.5 times interquartile range (75 minus

1150   25 percentile). The black curves represent spline through two UV and three VIS-NIR wavelengths. Note that the 660-nm SSA retrievals are interpolated using those at 470 nm and 860 nm. In-situ airborne measurements of SSA from PSAP and Nephelometer sensors for the respective ORACLES deployment years are shown as red box and whisker plots, whereas spectral SSA inversions from AERONET over inland stations are depicted using different symbols in black. Retrievals of spectral SSA from a research technique combining ground-based AERONET AOD measurements

1155   and satellite observations from OMI (354 nm and 388 nm) and MODIS (470 nm and 660 nm) over the inland site *Mongu* in *Zambia* are shown as blue asterisks; corresponding vertical dotted blue lines are the corresponding standard deviations.
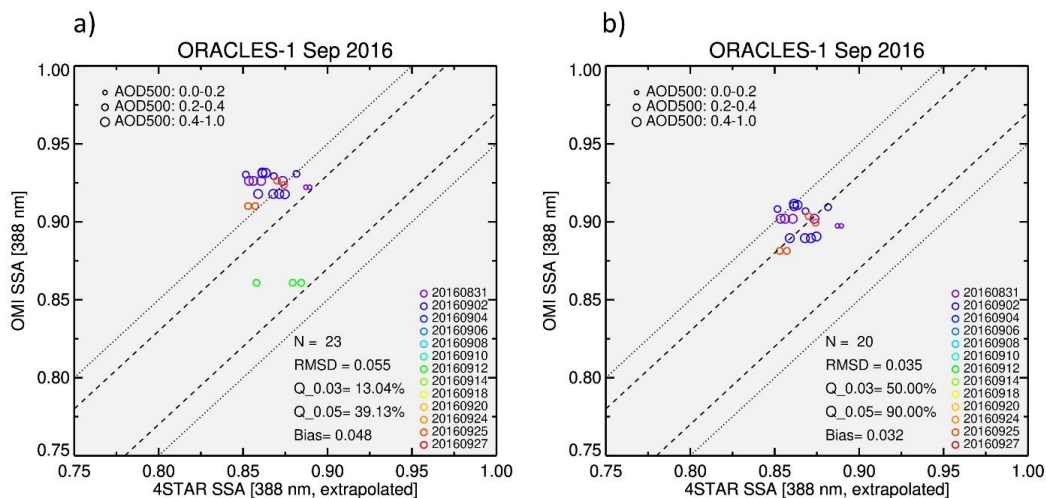
Figure 9. Comparison of spacetime collocated above-cloud aerosol SSA retrieved from OMI (388 nm) against those derived from 4STAR sunphotometer sky scan observations for the ORACLES-1 September 2016 campaign. The OMI SSA retrievals using the original aerosol model (a, left) with 20% relative spectral dependence in the imaginary part of the refractive index (AAE ~2.45-2.60) and modified aerosol model (b, right) with 10% spectral dependence in the imaginary index (AAE ~1.72-187) are evaluated against those of 4STAR inversions. The Q_0.03 and Q_0.05 are the % matchups falling within the relative difference of ±0.03 and ±0.05, respectively. The OMI-4STAR matchups are color-coded according to the date of observations shown in legends. The sizing of the circles corresponds to the magnitude of coincident AOD (500 nm). The statistical measures of the comparison are printed in the lower left of each plot.
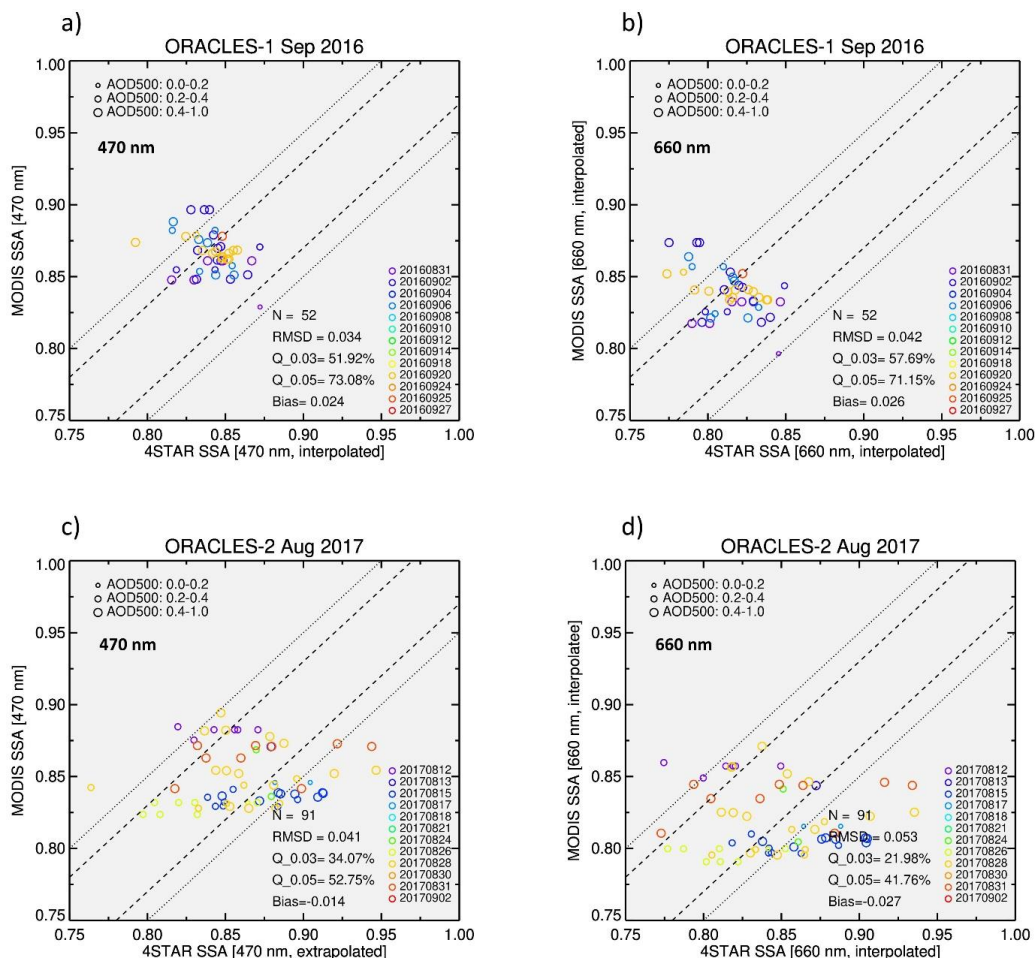
Figure 10. Comparison of spacetime collocated above-cloud aerosol SSA retrieved from MODIS at 470 nm (left column) and 660 nm (right column) against those derived from 4STAR sunphotometer sky scan observations for the ORACLES-1 September 2016 (a, b) and ORACLES-2 August 2017 (c, d) campaigns. The Q_0.03 and Q_0.05 are the % matchups falling within the relative difference of ±0.03 and ±0.05, respectively. The MODIS-4STAR matchups are color-coded according to the date of observations shown in legends. The sizing of the circles corresponds to the magnitude of coincident AOD (500 nm). The statistical measures of the comparison are printed in the lower left of each plot.
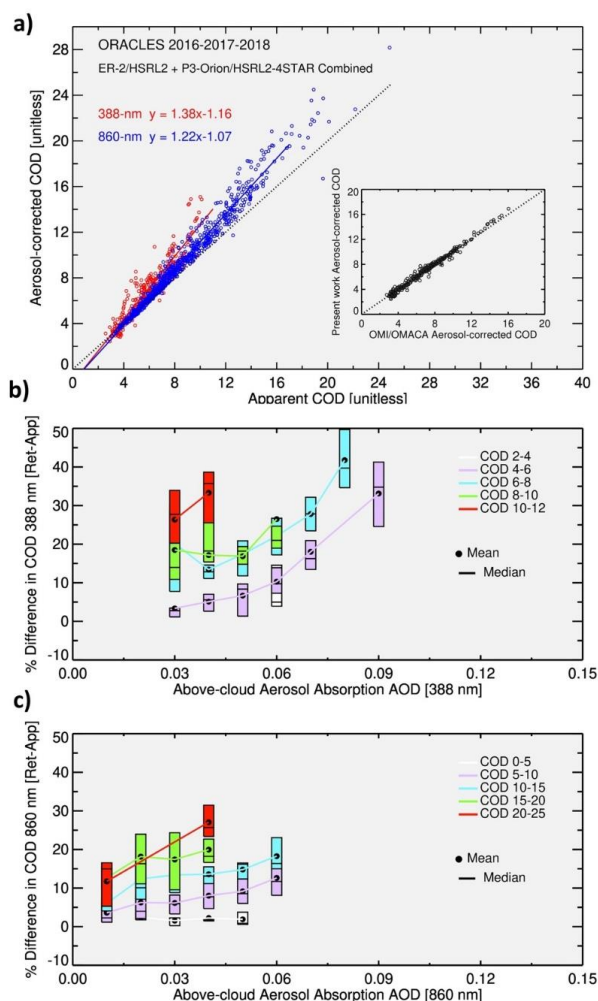
1180

Figure 11. a) A comparison of the aerosol-corrected (y-axis) and non-corrected (apparent) cloud optical depths retrieved from the present synergy algorithm at 388 nm (red) and 860 nm (blue). The combined retrieval dataset derived from HSRL-2 and 4STAR synergy with OMI and MODIS for all three years of ORACLES campaigns (2016, 2017, and 2018) is used. The solid lines represent linear regression fits calculated from OMI (red) and MODIS (blue)

1185 retrievals, respectively. A similar comparison graph shown in the inset relates the aerosol-corrected cloud optical depth retrieved from the present work (y-axis) with that obtained from the OMI-OMACA standard product. b) % difference in the COD (retrieved-apparent) at 388 nm of OMI as a function of above-cloud aerosol absorption AOD (388 nm), where each box represents 25 to 75 percentile data in AAOD bin size of 0.01. Different colors are used to denote data corresponding to different ranges of CODs. c) same as in (b) but for the 860 nm wavelength of MODIS.

1190

Figure 12. Uncertainty estimates of derived SSA at 388 nm (left) and 470 nm (right) calculated by contrasting the original OMI-MODIS-HSRL-2 collocated retrievals for the 2016 campaign against those retrieved using perturbed ACAOD (red), assumed aerosol layer height (ALH, blue), and relative spectral dependence in absorption or AAE (green). The absolute change in SSA was calculated as perturbed minus original retrievals.